Research on Chemical Intermediates
https://doi.org/10.1007/s11164-026-05936-x

Biofuel production from model bio-oil: impact of perovskite-based catalysts and metal oxide mixtures on upgrading and selectivity

Merve Celik Ozcan[1,2] · Doruk Dogu[3] · Nuray Oktar[1]

Received: 21 October 2025 / Accepted: 31 January 2026
© The Author(s) 2026

Abstract

Biofuel production was conducted using model bio-oil to examine the upgrading performance of perovskite-based and metal oxide catalysts. Bare and Ce, Co, Sr, Mo, and tungstophosphoric acid-doped $LaFeO_3$ perovskite-based catalysts were synthesized via sol–gel method. The bio-oil upgrading activity of commercial La_2O_3, α-Fe_2O_3, and α-Fe_2O_3/La_2O_3 metal oxide catalysts compared to $LaFeO_3$-based catalyst was also investigated. Catalyst properties were characterized by XRD, TGA/DTG, N_2 adsorption/desorption, SEM–EDX, FTIR, DRIFTS, and Raman techniques. Activity tests were performed at 400 °C at under atmospheric pressure. A model bio-oil mixture was formulated with hydroxy propanone/formic acid/furfural (2:4:3 mass ratio), and a dilution ratio of 30:70 (bio-oil mixture/alcohol) was applied. Ethanol and methanol were examined as co-reactants. Ethanol-assisted upgrading resulted in higher deoxygenation efficiency and enhanced iso-paraffin selectivity compared to methanol. Increasing the calcination temperature of $LaFeO_3$ from 700 to 800 °C improved crystallinity and raised the overall bio-oil conversion from 69.4 to 83.4%. The bare $LaFeO_3$ catalyst calcined at 800 °C exhibited high iso-paraffin selectivity (69.4 vol%) and oil-phase selectivity (80.3%). The superior upgrading performance of $LaFeO_3$ was attributed to its orthorhombic perovskite lattice structure and mild surface acidity, favoring cracking, deoxygenation, and coke suppression. Ce-doped $LaFeO_3$ ($x=0.1$) enhanced oxygen mobility and promoted olefin selectivity resulting in the highest overall bio-oil conversion (83.8%). At higher Ce contents ($x=0.2$), CeO_2 side-phase formation promoted naphthene selectivity. In contrast, Sr-, Co-, and Mo-doped $LaFeO_3$ catalysts showed higher oxygenated content. Compared with α-Fe_2O_3/La_2O_3 mixed catalyst, which exhibited 16.0 wt% coke formation, $LaFeO_3$ showed low coke deposition (0.24 wt%). Long-term stability testing of $LaFeO_3$ revealed only a very small amount of carbon formation (1.39 wt%) and no catalyst deactivation. Similar product distributions were obtained in both short-term and long-term tests.

Extended author information available on the last page of the article

Published online: 18 February 2026

Graphical abstract

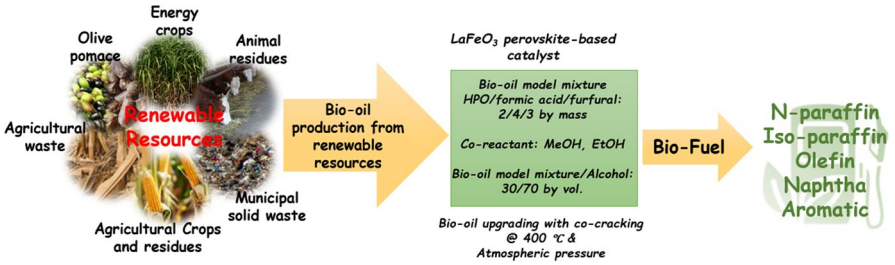

Keywords $LaFeO_3$ · Perovskite · Biofuel · Gasoline · Bio-oil · Iso-paraffin

Introduction

The depletion of fossil fuel reserves and rising environmental concerns have accelerated research on sustainable and alternative energy sources. Biomass, as a renewable and abundant feedstock, has gained significant interest for producing biofuels that can replace conventional transportation fuels. Among the various biofuel types, bio-oil produced through the fast pyrolysis of biomass has emerged as a promising candidate due to its high energy density and suitability for large-scale production [1, 2]. Bio-oil is a potential substitute for conventional fuels like gasoline and diesel. However, the direct application of crude bio-oil as a fuel is hindered by its undesirable properties, such as high oxygen and water content, high viscosity, corrosiveness, and low heating value [2, 3]. To overcome these limitations, catalytic upgrading processes such as hydrodeoxygenation and catalytic cracking have been employed to convert bio-oil into liquid hydrocarbon fuels similar to gasoline and diesel [1, 2].

The primary reactions expected to occur during upgrading include cracking, decarboxylation, deoxygenation, hydrocracking, and hydrogenation reactions [4]. The products obtained from the cracking zeolite-assisted response consist of three phases: gas phase, oil phase, and aqueous phase. The oil phase contains high-molecular-weight hydrocarbons with desired fuel properties, while the aqueous phase includes unconverted oxygenates and water. The gas phase mainly consists of CH_4, CO, and CO_2 [5].

Among these, catalytic cracking over zeolite-based catalysts, particularly HZSM-5, has emerged as a preferred method due to its ability to remove oxygen in the form of CO, CO_2, and H_2O without the need for external hydrogen [2, 6]. However, the complex and highly oxygenated nature of crude bio-oil, consisting of various components such as acids, ketones, alcohols, and phenols, complicates the cracking process. These components have different reactivities with some, such as phenols, leading to rapid catalyst deactivation through coke formation [3, 7]. The cracking potential of compounds in bio-oil content and the fuel phase yield are associated

with $(H/C)_{eff}$, which is an important indicator of the bio-oil chemical characteristics, as shown in Eq. (1) [1].

$$(H/C)_{eff} = \frac{[H] - 2[O] - 3[N] - 2[S]}{[C]} \quad (1)$$

Bio-oil derived from biomass pyrolysis has a low $(H/C)_{eff}$ value due to its high oxygen content and unsaturation of bio-oil subcomponents. This makes bio-oil less hydrogen-rich than other fuels, complicating its conversion into usable biofuels. The main challenge in upgrading bio-oil via catalytic cracking is to minimize coke deposition on the catalyst and increase oil yield. However, catalytic cracking of biomass pyrolysis-derived feedstock results in significant coke deposition. This issue is linked to the low $(H/C)_{eff}$ value of biomass-derived feedstock, which is mostly caused by their high oxygen content [8]. The higher this ratio, the easier the bio-oil is to process into biofuels. Innovative approaches such as co-cracking with alcohols (methanol or ethanol), mild hydrogenation, and molecular distillation have been proposed to overcome these challenges. Moreover, co-cracking of bio-oil with alcohols, such as ethanol or methanol, has been demonstrated to improve the selectivity for hydrocarbons by increasing the overall hydrogen-to-carbon ratio (H/C_{eff}) of the feedstock [2, 6]. Thus, the integration of co-cracking, molecular distillation, and mild hydrogenation represents a significant advancement in bio-oil upgrading, with the potential to produce high-quality liquid fuels while alleviating common problems such as catalyst deactivation and coke formation [3, 7].

Recent studies have investigated various metal oxide modifications (e.g., Ga_2O_3, ZnO, CuO) to improve the acidity and pore structure of HZSM-5, thereby enhancing the production of aromatic hydrocarbons, key components of high-quality gasoline [6]. Ibarra et al. focused on the catalytic cracking of bio-oil under fluid catalytic cracking (FCC) conditions using HY, HZSM-5, and Hβ zeolites, highlighting the role of acidity and shape selectivity. All catalysts achieved high deoxygenation efficiencies (61.1–80.4%), which increased with catalyst loading. HY maximized gasoline yield (46–55 wt%), HZSM-5 favored LPG production (12–14 wt%), while Hβ provided the highest total hydrocarbon yield (56 wt%) [9]. Cai et al. carried out hydrogenation at 200–250 °C on Ni–Cu/SiO_2 under 4 MPa and performed cracking at 400 °C on HZSM-5. High aromatic hydrocarbons were obtained when the simulated distillation fraction (SDF) of bio-oil was blended with 30% methanol. SDF mixture contained hydroxypropanone (HPO), cyclopentanone (CPO), and acetic acid (HAc). HPO and CPO showed high selectivity toward aromatics, whereas HAc mainly produced an aqueous phase and coke. HPO and CPO showed almost complete conversion (~99%), while HAc showed low conversion (57.4%) limited by its low reactivity [10]. Guvenc et al. conducted the catalytic upgrading of a model bio-oil model mixture in the presence of γ-Al_2O_3-based Ni, Ta, and Zr catalysts. The optimum co-cracking temperature was determined as 400 °C. The highest iso-paraffin selectivity and overall conversion value in the fuel phase were achieved in the presence of 10Zr@MA as 80.96% and 92%, respectively. Also, it has been observed that Brønsted acid sites affect the selectivity of iso-paraffins, while the presence of Lewis acid sites triggered the selectivity of the olefin [11]. In

bio-oil upgrading through catalytic cracking, catalyst stability is directly linked to coke deposition, which represents the primary cause of catalyst deactivation [12]. The presence of mild to moderate acidity in the catalyst is crucial for promoting deoxygenation and cracking reactions. The use of bio-oil components with high surface acidity and low H/C_{eff} ratios triggers coke formation. In this context, it has been observed that the use of catalysts with mild or moderate acidity supports deoxygenation and cracking [11, 13]. The specific surface area of the spent catalysts decreased markedly (from 269.4 to 16.2 m^2/g) due to pore blockage caused by coke deposition [5]. Ozcan et al. examined the type and amount of active metal in the catalyst and the effect of the impregnation sequence on biofuel production. Zr, Co, and W containing Al_2O_3 supported catalysts using the wet impregnation method synthesized. Bio-oil was represented by a mixture of model molecules that contained HPO, formic acid, and furfural (by mass in a ratio of 2:4:3). The co-impregnated 5Co-10Zr@MA catalyst showed high activity, with bio-oil conversion of 95% and iso-paraffin selectivity of 93%. The coke accumulation on 5Co-10Zr@MA was obtained as 2.8 wt%. The $CoAl_2O_4$ alloy exhibited high catalytic activity and improved resistance to coke formation [13]. In another study using the same bio-oil composition, Ni- and Co-loaded HZSM-5 catalysts demonstrated 77–84% conversion during bio-oil upgrading, where Ni favored paraffin/olefin formation and Co reduced coke formation [14]. HZSM-5 zeolite, a widely used microporous catalyst containing both Lewis and Brønsted acid sites, is preferred in alternative fuel production studies due to its high surface acidity [2, 3, 6, 11]. However, the combination of high acidity and a narrow microporous structure in HZSM-5 often promotes carbon deposition and diffusion limitations, thereby limiting its catalytic performance.

Because of its many physical and technological characteristics, such as ferroelectricity, piezoelectricity, pyroelectricity, high-temperature superconductivity, magnetic behavior, and catalytic activity, perovskite-type oxides have emerged as the most attractive candidate. These characteristics enable the use of such materials in various applications, including catalysts, gas converters, magnetic sensors, and solid-state electrolyte batteries. Perovskite oxide materials are well known for various catalytic applications, including bio-oil steam reforming, cracking reactions [15–18], partial oxidation of methane [19], CO_2 reforming of methane [20], biogas dry reforming [21], and the removal of nitrogen oxides (NO_x) [22]. $LaFeO_3$ has recently gained significant attention among perovskite-type oxides due to its catalytic and electrochemical capabilities [23]. $LaFeO_3$ is one of the important perovskites widely used in various applications, including solid oxide fuel cells, sensors, oxygen-permeable membranes, and catalysts [24].

Perovskite oxides have a general formula expressed as ABO_3. In the perovskite structure, 'A' represents lanthanide or alkaline earth metals, while 'B' denotes transition metals. The favored dopants for the A-site can typically include lanthanide elements such as La, Ce, Pr, Nd, Sm, Eu, Gd, or alkaline earth metals such as Sr, Mg, Ca, and Ba. Suitable transition metals for the B-site can include Fe, Ni, Co, Ti, Mn, Zn, Cu, Al, Cr, Y, Zr, W, Mo, Pd, Pt, and their various combinations [25]. By incorporating multiple metal dopants at both the A-sites and B-sites of the perovskite oxide structure, the ionic and electrical conductivity, structural

properties, stability during reactions, and overall performance of the catalyst can be enhanced. Considering the formula of the perovskite developed via doping as $A_{1-x}A'_xB_{1-y}B'_yO_3$, the A- and A'-sites consist of lanthanides and alkaline earth metals, respectively, and B and B'-sites are composed of transition metals [25, 26]. Within the scope of this study, metals such as Ce, Co, Mo, W, and Sr were incorporated into the $LaFeO_3$ perovskite catalyst structure to promote bio-oil upgrading through co-cracking.

The partial doping of cerium (Ce) into the A-site of the perovskite lattice facilitates the introduction of oxygen vacancies into the structure, thereby enhancing oxygen mobility [27]. In recent years, cerium oxide has emerged as a promising catalyst owing to its distinctive physicochemical properties, including a cubic crystal structure, rapid and reversible Ce^{4+}/Ce^{3+} redox cycles, stability under a wide range of temperature and pressure, and high oxygen storage and release capacity. The high mobility of oxygen vacancies plays an important role in any catalytic or electrochemical application. Adding trivalent Ce^{3+} ions to the perovskite crystal matrix causes the formation of oxygen vacancies. These vacancies enhance oxygen diffusion, increasing the material's ability to easily store and release oxygen [28]. The effect of copper (Cu) or cerium (Ce) as promoters for NiMo/γ-Al_2O_3 catalyst on the hydrodeoxygenation (HDO) of guaiacol (GUA) was investigated. It has been reported that electron migration from CeO_2 increases the electron density on Ni^0, thereby suppressing CH_4 formation which is identified as a key precursor to coke deposition on the catalyst surface [29]. Molybdenum (Mo)-containing catalysts such as Ni–Mo or cobalt (Co)–Mo supported on γ-Al_2O_3 catalysts are widely used in the hydrodeoxygenation upgrade process of bio-oils [30]. The hydrodeoxygenation of fatty acid esters was investigated by preparing Ni–Cu–Mo/Al_2O_3 catalysts with different Ni/Mo ratios. Mo (especially the Mo^{4+} form) directly increased the degree of complete deoxygenation (removal of oxygen) of the esters and thus the hydrocarbon alkane yield [31]. In the catalytic pyrolysis of cellulose with methanol as hydrogen donor, La–Ce/MCM-41 catalysts showed the best catalytic activity due to synergistic interaction of La–O and Ce–O species and the suitable mild strong acidity [32]. Tungsten (W) is theoretically employed as a promoter that enhances cracking capacity by strengthening Brønsted acid sites while suppressing Lewis acidity, which is responsible for coke formation, thereby reducing coke deposition [13]. The addition of cobalt has been shown to improve both the activity and stability of the catalyst [13, 33]. Cheng et al. investigated the hydrodeoxygenation (HDO) upgrading of pine-sawdust-derived bio-oil over bimetallic Fe–Co/SiO_2 catalysts. It is reported that the bimetallic system outperformed the monometallic catalysts due to the synergistic interaction on the SiO_2 support. The Fe–Co/SiO_2 catalyst, characterized by moderate acidity, showed higher efficiency in bio-oil upgrading. In contrast, the Co/HZSM-5 catalyst produced a lower biofuel yield (14.43 wt%) compared to Fe-Co/SiO_2 (23.85–33.91 wt%) [34]. Perovskite oxides, with their uniquely tunable bulk composition and versatile surface properties, exhibit excellent thermal stability and sustained catalytic activity over a wide temperature range. Sr-doped $LaNi_{0.8}Fe_{0.2}O_3$ catalysts were used on Linfen coal and bamboo sawdust co-pyrolysis. Doping of Sr promoted the formation of defects and oxygen vacancies in the structure. $La_{1-x}Sr_xNi_{0.8}Fe_{0.2}O_3$ with a doping level of $x=0.3$ exhibited the strongest synergistic interaction with the pyrolysis volatiles, achieving the highest syngas yield with an

H_2/CO ratio of 3.98 [35]. Doping at A/B sites can effectively improve the catalytic activity. Synergistic interactions among the multiple active sites of perovskite catalysts play a decisive role in the product distribution. Furthermore, $LaFeO_3$ exhibited a strong deoxygenation capability during the catalytic pyrolysis of industrial lignin. This behavior is attributed to active oxygen vacancies that promote the adsorption of oxygenated species, C–O bond cleavage, and aromatization, thereby improving bio-oil quality [36]. $LaFeO_3$-based catalyst is an effective catalyst and oxygen carrier for the cracking and reforming of biomass-derived tars and hydrocarbons, thereby standing out for its ability to promote syngas and hydrogen production [37, 38].

Based on the reviewed literature, extensive research has been undertaken to explore the potential of bio-oil as an alternative fuel and to enhance the selectivity of high-value-added products through upgrading processes. The present study focuses on developing novel, next-generation perovskite-based catalysts that demonstrate stable performance in co-cracking reactions and exhibit high resistance to coke formation. In the present study, bare and Ce, Co, Sr, Mo, and TPA (tungstophosphoric acid)-doped $LaFeO_3$ catalysts were prepared by the sol–gel method, and their performance in bio-oil upgrading was investigated. The upgrading activity of commercial La_2O_3, α-Fe_2O_3, and α-Fe_2O_3/La_2O_3 metal oxide mixture catalysts was also investigated. Biofuel production from bio-oil via co-cracking reaction in the presence of co-reactant ethanol at 400 °C under atmospheric pressure was performed. A model mixture with a fixed composition was employed to simulate the bio-oil mixture. Hydroxy propanone (HPO), representing ketones, furfural, representing furans, and formic acid, representing acids, were selected as key subcomponents to represent the chemical composition of bio-oil. To increase the $(H/C)_{eff}$ value of the mixture, which plays a role in the stability of the cracking process, the mixture was diluted with ethanol ($(H/C)_{eff}$:2). The effect of methanol as a co-reactant on the $LaFeO_3$ catalyst was also investigated. The bio-oil model mixture was prepared at a 2:4:3 mass ratio of HPO/formic acid/furfural. The co-cracking reaction was carried out with the reactant feed ratio of 30:70 bio-oil/alcohol (v/v). Thus, it aims to contribute to developing a sustainable and efficient biofuel production process by investigating the effects of perovskite catalysts on the conversion of model bio-oil components and increasing biofuel selectivity and quality. This study investigates the catalytic performance of compositionally tunable $LaFeO_3$-based perovskites with different metal dopants in the alcohol-assisted co-cracking of a bio-oil model mixture. It further highlights these tailored catalysts, designed to improve resistance to coke formation, as a promising approach for effective bio-oil upgrading. Moreover, this study offers a new perspective on the application of perovskite catalysts in fuel technologies derived from renewable resources.

Experimental

Catalyst preparation

The synthesis of high-purity crystalline perovskite-based materials is achieved through various techniques, including sol–gel, hydrothermal, co-precipitation, and template methods. There are also recipes for perovskite-based materials using

multi-step synthesis procedures such as the complexation method or the Pechini route [39, 40]. Among these, the sol–gel method is the most widely employed for preparing perovskite nanoparticles. This method offers several advantages, such as ease of operation, low cost, and high purity. Furthermore, it enables precise control over surface properties, particle size, and morphology [23, 24, 41]. In this study, a perovskite-based catalyst was synthesized by the sol–gel method by modifying the recipes in the literature [27, 42, 43]. The general chemical formula of perovskite is defined as ABO_3. Metal dopings in the perovskite structure were made on both A and B sides ($A_{1-x}A'_xB_{1-y}B'_yO_3$). In case A and B sides are La and Fe, respectively, different dopings were applied to the $LaFeO_3$ structure as A': Ce, Sr and B': Co, Mo, W, P. Pure and different metal-doped lanthanum–ferrite perovskite oxide catalysts, $La_{1-x}A'_xB_{1-y}Fe_yO_3$ ($1-x=1.0$, 0.9, 0.8, 0.1 and $1-y=1.0$, 0.9), were prepared via a sol–gel method. To prepare the pure $LaFeO_3$, stoichiometric amounts of $La(NO_3)_2{\cdot}6H_2O$ (99.99%, Merck) and $Fe(NO_3)_3.9H_2O$ (99.9%, Merck) were measured and dissolved in 25 mL of deionized water at 30 °C and 275 rpm. For the synthesis of metal-doped $LaFeO_3$ catalysts, the metal salt solution was prepared in the same way using metal sources ($Ce(NO_3)_3.6H_2O$, 99.9%, Sigma-Aldrich, as cerium source; $Sr(NO_3)_2$, Alfa Aesar, as strontium source; $(NH_4)_6Mo_7O_{24}.4H_2O$, Merck, as molybdenum source; $Co(NO_3)_2.6H_2O$, Merck, as cobalt source; tungstophosphoric acid hydrate-TPA, $H_3O_{40}PW_{12}xH_2O$, Merck, as tungsten source) in stoichiometric ratio. The aqueous solution was placed in a water bath, and the temperature was raised to 60 °C. Citric acid (ACS reagent ≥ 99.5%, Sigma-Aldrich) is used as a gelling agent. A citric acid solution is prepared in an equimolar ratio (1:1) with the total metal nitrates in the solution. A citric acid solution was added drop by drop to the aqueous metal solution at 60 °C under continuous stirring at 275 rpm. Then, the gelation process (aging) of the solution was provided at 80 °C. A drying process is applied in the oven at 130 °C for 12 h. After drying, dark brown a cake-like structure is obtained and is ground into powder using a mortar. The perovskite catalyst was calcined with a heating rate of 5 °C/min under dry air flow for 4 h. To obtain the La_2O_3 metal oxide phase, calcination processes were carried out at different temperatures (700 °C, 900 °C) and in the atmosphere (helium, steam + helium, dry air). Calcination studies were carried out using commercial lanthanum nitrate hexahydrate salt (LaNH, $La(NO_3)_2.6H_2O$, 99.99%, Merck) and commercial La_2O_3 powder (BDH Chemicals Ltd.). Since La_2O_3 is unstable under ambient conditions, the La_2O_3 phase was tried to be obtained from $La(OH)_3$ phase at appropriate calcination temperature and in the environment. The samples were kept in a desiccator without contact with air. The catalysts used within the scope of the study, the catalyst preparation method, and calcination parameters are presented in Table 1.

Catalyst characterization

The synthesized materials were characterized by thermogravimetric/derivative thermogravimetry (TG/DTG), X-ray diffraction (XRD), N_2 adsorption/desorption, scanning electron microscopy (SEM), Fourier transform infrared spectroscopy

(FTIR), and pyridine-adsorbed diffuse reflectance FTIR spectroscopy (DRIFTS). After the activity tests, coke formation in spent catalysts was also investigated using the thermogravimetric (TG) analysis, XRD techniques and Raman spectroscopy. XRD analysis was conducted by Bruker D2 Phaser diffractometer with a CuKα ($\lambda = 0.15406$ nm) radiation source. Diffraction patterns were recorded in 2Theta scanning from 10° to 90° using a scanning speed of 2°/min. TG/DTG analyses of uncalcined catalysts were performed with the HITACHI STA 7300 simultaneous thermogravimetric analyzer under dry airflow from 30 to 900 °C at a heating rate of 5 °C/min. The BET surface area, average pore diameter, and pore volume of the catalyst were determined by nitrogen adsorption–desorption analysis using a Micromeritics Tristar II 3020 instrument. Before the analysis, all samples were dried and degassed under vacuum at 250 °C for 3 h. Measurements were carried out at various relative nitrogen pressures at 77 K. The relative pressure (P/P_0) was varied during the measurements between 10^{-5} and 0.99. SEM analysis was used to determine the morphological structure of the catalysts. SEM images were obtained by JEOL JSM-7001 FLV TTLS instrument. FTIR analysis of catalyst was carried out by attenuated total reflection (ATR) technique in the range of 4000–400 cm^{-1} using JASCO Model FT/IR-4700. DRIFTS of pyridine-adsorbed catalysts was conducted using a JASCO FT/IR-4700 spectrometer to characterize the relative strength of surface acid sites. TGA of the spent catalysts was performed using a Perkin Elmer Pyris 1 instrument to determine the amount of coke deposition on the catalyst's surface. The analysis was conducted under both dry air and nitrogen flow from 30 to 900 °C, with a heating rate of 10 °C/min. Raman spectroscopy was conducted to determine coke formation of spent catalysts using JASCO NRS4500 confocal with 532 nm laser.

Table 1 Catalyst preparation methods and parameters

Catalyst	Catalyst preparation method	Calcination parameters
$LaFeO_3$ (700 °C)	Sol–gel	700 °C, dry air
$LaFeO_3$ (800 °C)	Sol–gel	800 °C, dry air
$La_{0.9}Ce_{0.1}FeO_3$	Sol–gel	800 °C, dry air
$La_{0.8}Ce_{0.2}FeO_3$	Sol–gel	800 °C, dry air
$LaFe_{0.9}Co_{0.1}O_3$	Sol–gel	800 °C, dry air
$LaFe_{0.9}Mo_{0.1}O_3$	Sol–gel	800 °C, dry air
$LaFe_{0.9}W_xP_yO_3$	Sol–gel	800 °C, dry air
$La_{0.9}Sr_{0.1}FeO_3$	Sol–gel	800 °C, dry air
$La_{0.1}Sr_{0.9}FeO_3$	Sol–gel	800 °C, dry air
$La_{0.8}Ce_{0.2}Fe_{0.8}Co_{0.2}O_3$	Sol–gel	800 °C, dry air
α-Fe_2O_3	Commercial	–
La_2O_3	Commercial	900 °C, Helium
α-Fe_2O_3/La_2O_3	Physical mixing	(La/Fe = 1:1 molar ratio)

Catalytic activity tests

The bio-oil upgrading tests were performed using a quartz tubular reactor with an inner diameter of 6 mm. Before the upgrading studies, calcined catalyst powders were pelletized between 1 and 2 mm, and then 0.5 g of catalyst was placed in the center of the quartz reactor. Ethanol ($C_2H_5OH, \geq 99.9\%$, Merck) was used to upgrade bio-oil model compounds as a diluent and co-reactant. All activity test studies were conducted at atmospheric pressure and 400 °C for 3 h. Quartz wool was used at both ends of the reactor to fix the catalyst bed. The bio-oil model compound was prepared by mixing 2:4:3 constant ratio by mass using HPO ($C_3H_6O_2$, 95%, Alfa Aesar), formic acid (CH_2O_2, 98–100%, Merck), and furfural ($C_5H_4O_2$, 99%, Sigma-Aldrich), respectively. The reactant mixture was prepared using a model bio-oil mixture combined with co-reactant alcohols (ethanol and methanol) at a volumetric ratio 30:70 and introduced at a mixture flow rate of 0.25 mL/min via an HPLC pump. Subsequently, the mixture was evaporated in an atmospheric evaporator at 200 °C. Helium, the carrier gas at a 60 mL/min flow rate, was co-fed with the bio-oil mixture to the vaporizer. To prevent condensation, the pipelines at the upgrading setup were heated to 200 °C with heater tapes. The gas mixture formed during the reaction (CO, CO_2, CH_4, C_2H_4, C_2H_6, C_3H_6, C_3H_8) was passed through the condenser and then reached the gas chromatograph (Agilent Model 6890 N), which was equipped with a thermal conductivity detector (TCD) and Porapak-Q packed column. Condensable products and unreacted compounds were collected in the glass condenser at the reactor outlet. The collected oil-phase products were analyzed to determine the hydrocarbon distribution using a flame ionization detector (FID) and HP-1 capillary column. Quantitative analysis of hydrocarbon-containing samples was performed using the Detailed Hydrocarbon Analysis Program (DHA). The experimental setup used for biofuel production is given in Fig. 1.

The definitions of bio-oil conversion (Eq. (2), Eq. (3)), gas-phase product distribution (Eq. (4)), oil and aqueous phase selectivity (Eq. (5), Eq. (6)), and yield (Eq. (7)) used in our previous studies are presented in detail [11, 13, 44]. Yield is defined as the fraction of converted reactants that are ultimately transformed into the target oil-phase products. This parameter is calculated by multiplying the overall conversion of the feedstock by the corresponding selectivity toward the oil phase.

$$X_i = \frac{(\mathrm{Fi})\mathrm{in} - (\mathrm{Fi})\mathrm{out}}{(\mathrm{Fi})\mathrm{in}} \times 100 \tag{2}$$

$$X_{\text{overall (HPO+fulfural+FA+EtOH)}} = \frac{(\mathrm{Fo})\mathrm{in} - (\mathrm{Fo})\mathrm{out}}{(\mathrm{Fo})\mathrm{in}} \times 100 \tag{3}$$

$$y_{i,\mathrm{gas}} = \frac{(Fi)}{(F)\mathrm{total}} \times 100 \tag{4}$$

$$S_{\text{oil phase}} = \frac{(m_{\text{oil phase}})_{\text{collected}}}{(m_{\text{reactants}})_{\text{in}} - (m_{\text{reactants}})_{\text{out}}} \times 100 \tag{5}$$

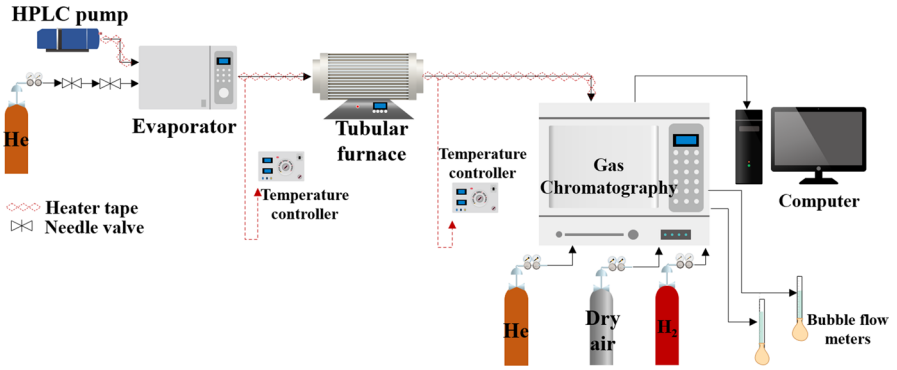

Fig. 1 Experimental Setup for Biofuel production from Bio-oil

$$S_{\text{aqueous phase}} = \frac{(m_{\text{aqueous phase}})_{\text{collected}}}{(m_{\text{reactants}})_{\text{in}} - (m_{\text{reactants}})_{\text{out}}} \times 100 \tag{6}$$

$$\text{Yield} = (X_{\text{overall}} * S_{\text{oil phase}})/100 \tag{7}$$

Results and discussion

Catalyst characterization

In this study, pure and metal-doped $LaFeO_3$ perovskite catalysts were synthesized via the sol–gel method and subsequently characterized. To evaluate the activity of pure $LaFeO_3$ in comparison with mixed metal oxides, a complementary investigation was conducted to synthesize the La_2O_3 metal oxide phase. The structural properties of the perovskite-type catalysts, along with their influence on model bio-oil conversion and biofuel selectivity, were systematically examined. Furthermore, the catalytic performance of the $LaFeO_3$ co-cracking catalyst was compared stoichiometrically with that of a mixed oxide catalyst (α-Fe_2O_3/La_2O_3) containing equivalent metal content. The physical properties of the synthesized catalytic materials were analyzed through various characterization techniques to provide comprehensive insights into their catalytic behavior.

To determine the calcination temperature of the catalysts synthesized by the sol–gel method, TG-DTG analysis was performed for pure $LaFeO_3$ before calcination. The TGA/DTG result of pure $LaFeO_3$ perovskite is given in Fig. 2. The initial weight loss below 150 °C could be attributed to the evaporation of water. The weight losses are due to the decomposition of iron nitrate in the temperature range of 150–270℃, the decomposition of organic matter in the temperature range of 270–340 °C, the decomposition of lanthanum nitrate in the temperature

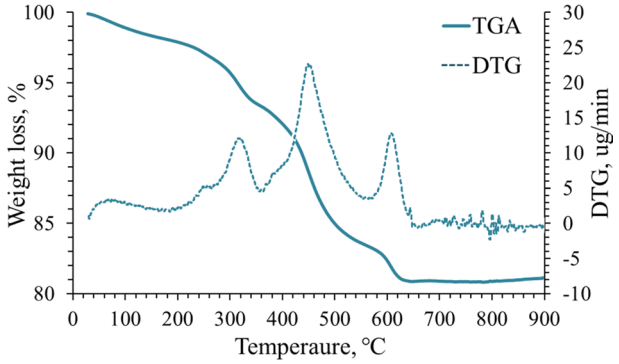

Fig. 2 TG and DTG analysis results of uncalcined bare $LaFeO_3$ perovskite

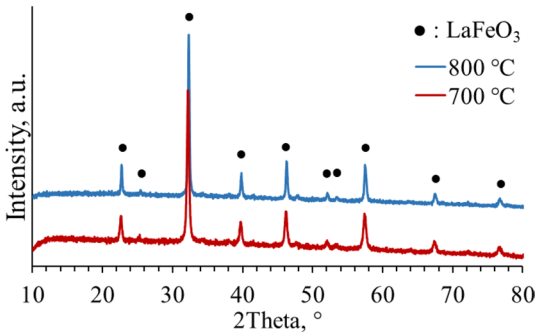

Fig. 3 Wide-angle XRD patterns of bare $LaFeO_3$ materials calcined at 700 °C and 800 °C

range of 340–550 °C, and the loss of oxygen resulting in the crystallization of $LaFeO_3$ up to 650 °C [42]. The weight change was fixed at 650 °C. TGA and XRD results were evaluated together to determine the calcination temperature.

XRD analysis was performed to investigate the effect of calcination temperature on the structure and determine the prepared material's crystal structure. The effect of calcination temperature on the structure was investigated in pure $LaFeO_3$ catalyst synthesis studies. XRD patterns (2 Theta 10–90° range) of pure $LaFeO_3$ materials calcined at different temperatures (700 °C and 800 °C) for 4 h under dry air are given in Fig. 3. In the literature, the XRD pattern of $LaFeO_3$ shows characteristic peaks at 2Theta values of 22.6°, 25.5°, 32.2°, 34.5°, 39.7°, 46.1°, 47.7°, 52.0°, 54.0°, 57.4°, 64.0°, 67.3° and 76.6°, which corresponds to (101), (111), (121), (210), (220), (202), (230), (141), (311), (240), (115), (242) and (204) diffraction planes, respectively (JCPDS: 88-0641) [45]. This study observed characteristic peaks associated with the $LaFeO_3$ (●) (COD: 1526450) phase in the XRD patterns of materials subjected to different calcination temperatures. As the calcination temperature increased, it was observed that there was an increase in the characteristic peak intensities and crystal size, indicating the orthorhombic lattice

structure of pure $LaFeO_3$. The study determined the calcination temperature for pure $LaFeO_3$ and metal-doped $LaFeO_3$ catalysts as 800 °C.

Metal (Ce, Co, Mo, Sr, and TPA)-doped $LaFeO_3$ catalysts were synthesized using the sol–gel method. In the study, Sr and Ce were doped on the A side of the $LaFeO_3$ perovskite structure, and Co, Mo, and TPA were doped on the B side. The calcination process of metal-doped $LaFeO_3$ catalysts ($La_{1-x}A'_xB_{1-y}Fe_yO_3$; $x=0.0$, 0.1, 0.2, 0.9; $y=0.8$, 0.9, 1.0) was carried out at 800 °C for 4 h under dry air. Wide-angle XRD patterns (2Theta: 10–80°) of perovskite-based catalysts are given in Fig. 4. In the XRD patterns, characteristic peaks corresponding to the $LaFeO_3$ phase (●) (COD: 1526450) were observed for pure and metal-doped $LaFeO_3$ catalysts. XRD patterns exhibited that in case of $0.0 \le x \le 0.10$ for the $La_{1-x}Ce_xFeO_3$, $LaFe_{0.9}Mo_{0.1}O_3$, $LaFe_{0.9}Co_{0.1}O_3$, $LaFe_{0.9}W_xP_yO_3$, and $La_{0.9}Sr_{0.1}FeO_3$ catalysts have a single-phase orthorhombic lattice structure in the patterns compatible with $LaFeO_3$(●) (COD: 1526450). It has been determined that $LaFeO_3$-based materials have a single-phase orthorhombic lattice structure for $0.0 \le x \le 0.1$ and $0.1 \le y \le 0.2$. A characteristic peak indicating the formation of cubic CeO_2 phase was observed at approximately 2Theta: 28.5° for $x=0.20$ in $La_{1-x}Ce_xFeO_3$, and $La_{1-x}Ce_xCo_{0.2}$ $Fe_{0.8}O_3$ catalysts (COD: 4343161 and JCPDS: 43-1002) [46, 47]. In the $La_{1-x}Ce_xFeO_3$ perovskite structure with $0 \le x \le 0.10$, it has been observed that the single-phase orthorhombic crystal structure of $LaFeO_3$ is maintained upon the addition of Ce. However, in studies conducted for $x \ge 0.20$, it has been reported that a cubic CeO_2 phase is formed in addition to the pure $LaFeO_3$ phase [48–51].

The angle of the diffraction peaks moved to the right, and the intensity of the diffraction peak decreased with high Sr^{2+} doping into the perovskite structure. The formation of the side phase was observed at approximately 2Theta: 32.8° in the $La_{0.1}Sr_{0.9}FeO_3$ catalyst. In Sr-doped ($x=0.9$) $LaFeO_3$, it was detected in secondary phase XRD data like $SrFeO_3$. The XRD pattern displayed diffraction peaks located at 23.1°, 32.8°, 40.4°, 47.1°, 58.3°, 68.6°, and 78.3° regarding $SrFeO_3$. This pattern signifies a pure cubic crystal structure for $SrFeO_3$, associated with ICSD ID 91062 and JCPDS card 46-0335. The intensity of the $SrFeO_3$ cubic phase perovskite peaks was notably sharp and strong, aligning with

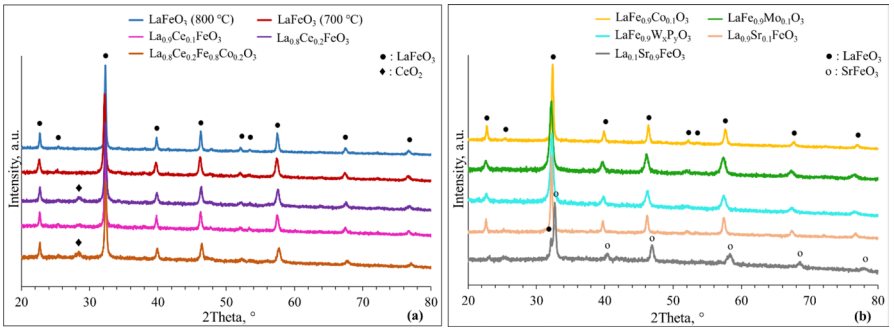

Fig. 4 Wide-angle XRD pattern of **a** bare $LaFeO_3$, Ce- and Ce-Co-doped $LaFeO_3$; **b** Co-, W-, Sr- and Mo-doped $LaFeO_3$ materials

previous studies' findings. Moreover, although the structure of $SrFeO_3$ is cubic, its diffraction pattern is close to $SrFeO_{2.97}$ (JCPDS card 40-0905) [52–55].

The crystal sizes of pure and metal-doped $LaFeO_3$ materials calculated from the Scherrer equation are given in Table 2. The Debye–Scherrer equation is given in Eq. (8)

$$D = \frac{K\lambda}{\beta \cdot \cos\theta} \tag{8}$$

where D represents the crystallite size, K is the Scherrer constant (taken as 0.89), λ is the wavelength of Cu-Kα radiation (0.15406 nm), β is the full width at half maximum (FWHM) of the diffraction peak, and θ is the Bragg angle corresponding to the diffraction peak. Increasing the calcination temperature from 700 to 800 °C resulted in a significant crystal growth of bare $LaFeO_3$, and the crystal size increased from 44.5 to 67.6 nm. This behavior is consistent with the enhanced sintering that occurs with increasing calcination temperature. In contrast, introducing various doping cations at 800 °C systematically suppressed crystal growth, and all metal-doped samples showed smaller crystallite sizes compared to bare $LaFeO_3$ (Table 2). In addition, it was determined that the crystal size of the highly Sr-doped $La_{0.1}Sr_{0.9}FeO_3$ catalyst was 40.95 nm at 2Theta 32.12° due to the formation of the $SrFeO_3$ main phase. The microstrain (ε), representing the lattice strain within the perovskite structure was evaluated using the simplified Williamson–Hall (W–H) equation (Eq. (9)).

$$\varepsilon = \frac{\beta}{4\tan\theta} \tag{9}$$

The lattice strain values estimated from the peak broadening reveal a clear correlation between dopant incorporation and crystal size reduction. While bare $LaFeO_3$ calcined at 800 °C exhibits relatively low microstrain, the introduction

Table 2 The crystal size and microstrain values of bare and metal-doped $LaFeO_3$ catalysts

Catalyst	Calcination temperature (°C)	2Theta (°)	FWHM (radian)	Crystal size (nm)	Microstrain ($\varepsilon \times 10^{-3}$)
$LaFeO_3$	700	32.15	0.18	44.5	2.73
$LaFeO_3$	800	32.29	0.12	67.6	1.81
$La_{0.9}Ce_{0.1}FeO_3$	800	32.29	0.15	54.9	2.26
$La_{0.8}Ce_{0.2}FeO_3$	800	32.33	0.17	47.6	2.56
$LaFe_{0.9}Co_{0.1}O_3$	800	32.37	0.18	46.8	2.71
$LaFe_{0.9}Mo_{0.1}O_3$	800	32.18	0.29	28.0	4.39
$LaFe_{0.9}W_xP_yO_3$	800	32.23	0.27	30.0	4.08
$La_{0.9}Sr_{0.1}FeO_3$	800	32.19	0.15	55.3	2.27
$La_{0.1}Sr_{0.9}FeO_3$	800	32.12	0.15	54.2	2.29
$La_{0.8}Ce_{0.2}Fe_{0.8}Co_{0.2}O_3$	800	32.32	0.18	45.5	2.71

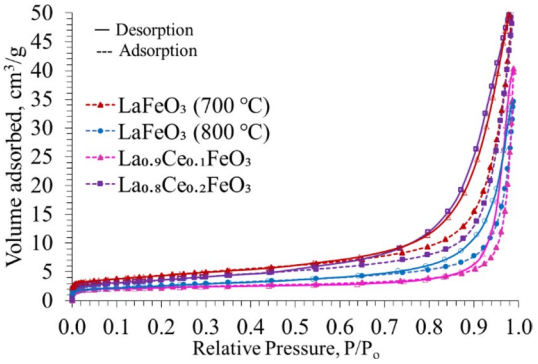

Fig. 5 N_2 adsorption–desorption isotherms of bare and Ce-doped $LaFeO_3$ catalysts

Table 3 Physical properties of the synthesized catalysts

Catalyst	Multi-point BET surface area, m^2/g	BJH desorption average pore diameter, nm	BJH desorption pore volume, cm^3/g
$LaFeO_3$ (700 °C)	15.23	13.2	0.081
$LaFeO_3$ (800 °C)	9.01	12.3	0.054
$La_{0.9}Ce_{0.1}FeO_3$	7.44	14.7	0.062
$La_{0.8}Ce_{0.2}FeO_3$	12.78	12.2	0.079

of hetero-cations systematically increases the strain within the perovskite lattice (Table 2). In particular, Mo- and W–P-doped samples show the highest strain levels ($4.08–4.39 \times 10^{-3}$), which is consistent with their smaller crystal sizes (28–30 nm). This behavior can be attributed to the aliovalent nature and ionic-size mismatch of the dopant cations, which induce lattice distortion, generate structural defects, and hinder crystal growth during calcination. Ce-, Co-, and Sr-doped samples also exhibit higher strain than bare $LaFeO_3$, supporting the conclusion that dopant-induced lattice distortion is a key factor suppressing crystal growth across all modified perovskites. The formation of oxygen vacancies and defects, which are more prevalent in smaller-crystal materials and those with higher microstrain, enhances oxygen mobility and related catalytic performance [56, 57].

N_2 adsorption/desorption isotherms of pure and Ce-doped $LaFeO_3$ catalysts are given in Fig. 5. The isotherms of synthesized perovskite materials were compatible with Type IV isotherms. The physical properties of pure and Ce-doped $LaFeO_3$ catalysts are given in Table 3. The interconnection of $LaFeO_3$ nanoparticles forms the mesoporous network in the materials. Hysteresis formation was observed at high relative pressures between the adsorption and desorption isotherms of the catalysts. H3 hysteresis occurred in the relative pressure range of 0.6–1.0 (P/Po) in all catalysts. The BET surface area values of the catalysts calcined at 800 °C varied from 9.01 to 12.78 m^2/g. It was observed that the catalyst surface area increased from $x = 0.10$ to $x = 0.20$ with the addition of Ce to the $LaFeO_3$ structure. It has been reported that this increase in surface area may be due to the separation of CeO_2 and Fe_2O_3 nanoparticles from perovskite oxide [48]. This observation was supported by

the XRD analysis results, which demonstrated that higher Ce loading in the $LaFeO_3$ nanoparticle structure reduces crystal size. Adding Ce resulted in smaller crystal sizes, accompanied by an increase in the catalyst's surface area. The BET surface area is primarily influenced by the particles' external surface and the nanoparticles' packing density, which is closely related to particle size. Accordingly, the increased BET surface area can be attributed to the smaller particle size. However, the overall surface area decreased, while the pore diameter in the $La_{0.9}Ce_{0.1}FeO_3$ perovskite structure increased. The increase in $La_{0.8}Ce_{0.2}FeO_3$ BET surface area was due to the separation of CeO_2 nanoparticles observed as a side phase from the perovskite oxide [48].

SEM–EDX elemental mapping of the samples is given in Fig. 6. The EDX mapping images of La, Fe, Ce, and O are indicated by different colors. SEM–EDX mappings of perovskite-type catalysts also clearly indicated homogeneous dispersion of all cations throughout the sample matrix. Elemental mapping confirmed the uniform distribution of La and Fe atoms event at the Ce doping. SEM images of fresh catalysts are given in Fig. 7. SEM investigated surface morphologies of pure $LaFeO_3$ and Ce-doped $LaFeO_3$ catalysts. For each sample, three different magnifications (20,000×; 70,000×; 100,000×) were reported. SEM analysis revealed that the particle size of Ce-doped $LaFeO_3$ is significantly smaller compared to the grain size of undoped $LaFeO_3$. A variation in particle sizes was observed across the samples, with particle sizes ranging from 29 to 63 nm. The incorporation of Ce into the $LaFeO_3$ structure led to a notable reduction in particle size. Additionally, Ce doping significantly decreased the interparticle pore density, particularly in the $La_{0.8}Ce_{0.2}FeO_3$ catalyst.

To examine the surface chemistry of the prepared perovskites, FTIR spectra were examined in the wavenumber range of 4000–400 cm^{-1} (Fig. 8a, b). The

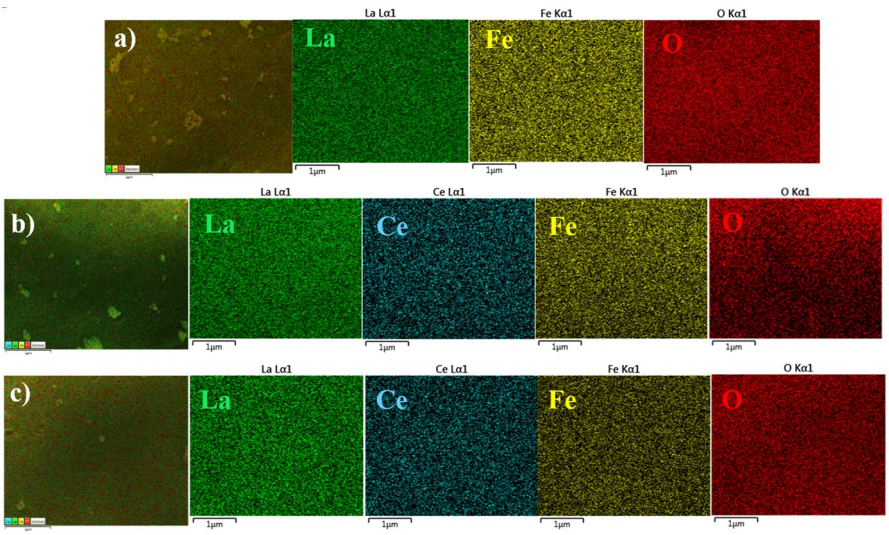

Fig. 6 SEM–EDX elemental mapping images of **a** $LaFeO_3$; **b** $La_{0.9}Ce_{0.1}FeO_3$; and **c** $La_{0.8}Ce_{0.2}FeO_3$

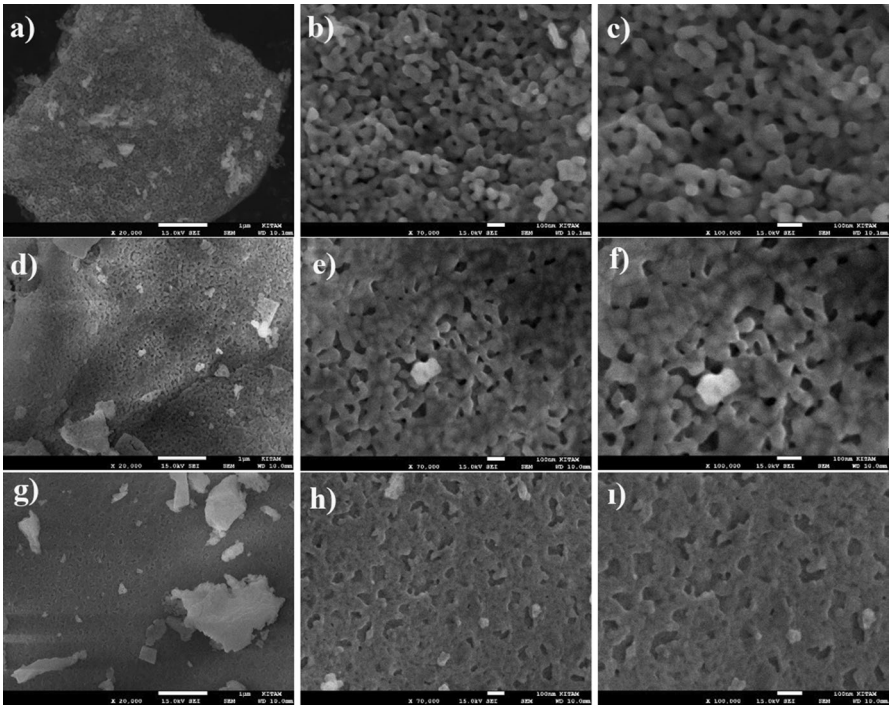

Fig. 7 SEM images of **a**–**c** $LaFeO_3$; **d**–**f** $La_{0.9}Ce_{0.1}FeO_3$; and **g**–**i** $La_{0.8}Ce_{0.2}FeO_3$

strong intensity band observed in the range of 700–400 cm^{-1} is assigned to the M–O the bending vibration and stretching vibration, thus revealing the formation of a metal–oxygen bond in the perovskite-based material [28]. The bands in the region of 730–504 cm^{-1} show the stretching modes of the octahedral FeO_6 groups in the perovskite lattice, which are the most important absorption bands of the perovskite structure [58]. In the catalysts prepared within the scope of the study, the

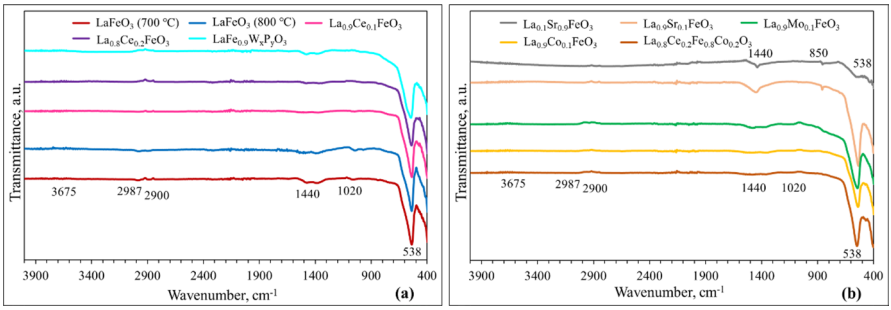

Fig. 8 FTIR spectra of **a** $LaFeO_3$ (700 °C), $LaFeO_3$ (800 °C), $La_{0.9}Ce_{0.1}FeO_3$, $La_{0.8}Ce_{0.2}FeO_3$, $LaFe_{0.9}W_xP_yO_3$; and **b** $La_{0.1}Sr_{0.9}FeO_3$, $La_{0.9}Sr_{0.1}FeO_3$, $LaFe_{0.9}Mo_{0.1}O_3$, $LaFe_{0.9}Co_{0.1}O_3$, $La_{0.8}Ce_{0.2}Fe_{0.8}Co_{0.2}O_3$

band observed at 538 cm^{-1} is due to the attribution of the Fe–O stretching vibrations formed by the octahedral FeO_6 group in $LaFeO_3$. The presence of a less intense band at 1018 cm^{-1} indicates the main vibration of the CO_3^{2-} group, which represents the presence of La-carbonate species on $LaFeO_3$ surface [59]. The bands at 1440 and 850 cm^{-1} are observed due to asymmetric and symmetric stretching and bending vibrations originating from CO_3^{2-} ($SrCO_3$) [60]. The bands at 2900 and 2987 cm^{-1} are due to adsorbed atmospheric CO_2 [59]. The absorption peak at 3675 cm^{-1} indicates a combination of the O–H stretching vibration of the hydroxyl group and the absorbed water [61, 62].

DRIFTS analysis of pyridine-adsorbed catalysts was performed to determine the strength and type of catalysts' acid sites. The relative densities of the Lewis and Brønsted acid sites were revealed by comparing the spectra of the fresh and pyridine-adsorbed catalysts. The spectra obtained in the wavenumber range of 1400–1650 cm^{-1} as a result of DRIFTS analysis of pyridine-adsorbed catalysts are given in Fig. 9a, b. In pyridine-adsorbed DRIFTS studies, it is observed that Lewis acidity gives peaks originating from coordinated pyridine at wavelengths of 1440–1460, 1488–1503, 1580, 1598, and 1600–1633 cm^{-1} [39, 63, 64]. Weak Brønsted acid sites are indicated by hydrogen-bonded pyridine, which gives bands in the range of 1440–1447, 1485–1490, and 1580–1600 cm^{-1} [39]. Furthermore, a literature review reveals strong Brønsted acidity is characterized by peaks at 1540 cm^{-1} and 1640 cm^{-1} [65]. The wavenumbers at 1489 and 1577 cm^{-1} indicate the Lewis and Brønsted acidity corresponding to the adsorption of pyridinium ions. The peaks of Lewis acid sites in the prepared catalysts were observed at 1444 and 1608 cm^{-1}. The peak at 1444 cm^{-1} indicates the presence of both Lewis and weak Brønsted acid sites in the catalyst. However, it represents a strong Brønsted acid site at wavenumbers of 1540 and 1640 cm^{-1}, but there is a very weak Brønsted acidity in the structure of the $LaFeO_3$ catalyst. When the absorbance peaks observed at the same wavelength at 1444 and 1596 cm^{-1} among the prepared catalysts are examined, it is seen that the highest absorbance peaks representing the Lewis acid site are formed in $LaFe_{0.9}Co_{0.1}O_3$, $LaFe_{0.9}Mo_{0.1}O_3$, and TPA-doped $LaFeO_3$ catalyst. A distinct acid site could not be observed in the Sr-doped $LaFeO_3$ and $La_{0.8}Ce_{0.2}Fe_{0.8}Co_{0.2}O_3$

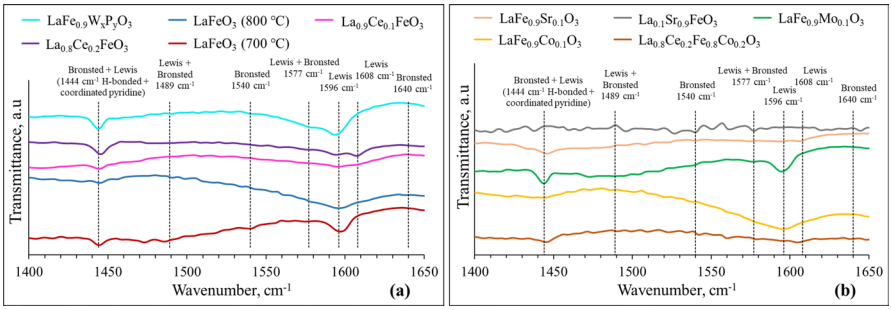

Fig. 9 Pyridine-adsorbed DRIFTS spectra of **a** $LaFeO_3$ (700 °C), $LaFeO_3$ (800 °C), $La_{0.9}Ce_{0.1}FeO_3$, $La_{0.8}Ce_{0.2}FeO_3$, $LaFe_{0.9}W_xP_yO_3$; and **b** $La_{0.1}Sr_{0.9}FeO_3$, $La_{0.9}Sr_{0.1}FeO_3$, $LaFe_{0.9}Mo_{0.1}O_3$, $LaFe_{0.9}Co_{0.1}O_3$, $La_{0.8}Ce_{0.2}Fe_{0.8}Co_{0.2}O_3$

catalysts. Absorbance peaks belonging to low-intensity Lewis acid sites were observed in pure and Ce-doped $LaFeO_3$ catalysts. In addition, tungstophosphoric acid (TPA), a type of heteropolyacid, was used as a W and P source to strengthen the Brønsted acid sites of the catalysts. Keggin-type heteropolyacids are known to strengthen the Brønsted acid sites of the catalyst. Heteropolyacids have very high thermal stability in the solid state. In Keggin type $H_3PW_{12}O_{40}$ (PW), $H_4SiW_{12}O_{40}$ (SiW), $H_3PMo_{12}O_{40}$ (PMo), and $H_4SiMo_{12}O_{40}$ (SiMo) structures, decompositions occur at temperatures of 465, 445, 375, and 350 °C, respectively [66]. This type of thermal decomposition results in the loss of acidity of HPAs [66, 67]. The DRIFTS results revealed that the Brønsted acidity associated with TPA contribution was weakly observed. TPA was directly doped to the $LaFeO_3$ structure, and the calcination process was applied at 800 °C. It is thought that a significant loss of acidity occurred at this temperature due to the loss of Keggin protons. In bio-oil upgrading processes, the presence of mild to moderate acidity in the catalyst is necessary for promoting deoxygenation and cracking reactions. However, strong acidic sites can accelerate coke deposition on the catalyst surface, ultimately diminishing catalytic performance [11, 13, 14].

In addition, studies were carried out under different temperatures and atmospheres to obtain the La_2O_3 metal oxide phase. When the TG-DTG results in the literature are examined, it is seen that the La_2O_3 phase can be obtained by removing water due to the dehydration and NO_2 from the structure in the decomposition temperature region of 70–660 °C. It was determined that the overall decomposition of LaNH was complete up to 660 °C. In the DTG curve of lanthanum nitrate hexahydrate salt ($La(NO_3)_2.6H_2O$, LaNH) decomposition, the evolution of water (H_2O) and nitrogen dioxide (NO_2) steps occurred [68]. In this study, LaNH salt was first calcined in dry air to obtain the La_2O_3 metal oxide phase. When the TG analysis results of the metal nitrate salt in the literature were examined, it was observed that the mass loss in the material remained constant after 660 °C [68]. Considering the TGA result for LaNH, the calcination process was carried out under dry air, helium and helium + water vapor flow for 5 h at a temperature of 700 ℃ with a temperature increase rate of 5 ℃/min. To obtain the La_2O_3 metal oxide phase, calcination was carried out in an inert gas environment as well as in a dry air environment. The wide-angle XRD patterns of the materials before and after calcination are given in Fig. 10. In the processes carried out with LaNH, it was determined that the peaks observed at 2Theta: 27.3°, 27.9°, 31.6°, 39.4°, 47°, 48.6°, 49.8°, 55.2°, 56.4°, 57.8°, 64.1°, 65.1°, 69.6°, and 77.4° belonged to the $La(OH)_3$ (●) (COD: 4031381) phase [69]. Therefore, it was determined that a higher calcination temperature should be increased to obtain a stable La_2O_3 metal oxide phase. The XRD pattern of the commercial La_2O_3 metal oxide material (COD: 2002286) was compared with the commercial La_2O_3 calcined at 900 ℃ with a temperature increase rate of 5 ℃/min for 5 h. The commercial La_2O_3 sample was calcined in an inert helium environment. It was determined that La_2O_3 is unstable under ambient conditions and transforms into the more stable $La(OH)_3$. Due to the hygroscopic structure of La_2O_3, it rapidly transforms into $La(OH)_3$ phase in a humid atmosphere by rehydroxylation [70, 71]. When the crystal size values calculated from the Scherrer equation in Table 4 are examined, lower crystal size was observed for LaNH in an inert environment

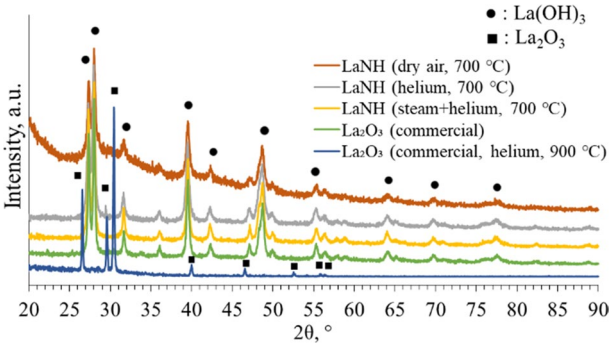

Fig. 10 Wide-angle XRD pattern of calcined LaNH and commercial La_2O_3 under different temperatures and atmospheres

compared to a dry air flow environment. After calcination, the crystal size of commercial La_2O_3 increased from 48.8 nm to 81.45 nm. XRD peaks belonging to the $La(OH)_3$ phase observed in commercial La_2O_3 samples before calcination prove that the structure is hygroscopic. The samples obtained after calcination were stored in sample containers with septum, preventing contact with the atmosphere, and kept in a desiccator. Commercial La_2O_3 calcined at 900 °C was used in the reaction studies.

Activity test results

The synthesis of biofuel from model bio-oil was performed at atmospheric pressure by using metal oxide and perovskite-type $LaFeO_3$-based catalysts. Alcohols (methanol and ethanol) and the model bio-oil mixture were preferred as co-reactants in the co-cracking reaction study. In previous co-cracking studies, it was observed that ethanol facilitates the conversion of ketones and acids into liquid aromatic hydrocarbons [1, 2, 6]. The ethanol/bio-oil model mixture's volumetric ratio was 70/30. In addition, the co-cracking study was carried out with a $LaFeO_3$ catalyst in the presence of methanol to examine the co-reactant effect. A constant alcohol/bio-oil:70/30 ratio was used. According to our earlier studies [11, 14], the maximum

Table 4 Crystal size values of calcined LaNH and commercial La_2O_3 under different temperatures and atmospheres

Catalyst	Calcination temperature (°C)	2Theta (°)	FWHM (radian)	Crystal size (nm)
LaNH (dry air, 700 °C)	700	28.0	0.19	44.7
LaNH (helium, 700 °C)	700	27.96	0.21	38.8
LaNH (helium + steam, 700 °C)	700	28.0	0.14	60.0
La_2O_3 (commercial)	–	28.05	0.17	48.8
La_2O_3 (commercial, helium, 900 °C)	900	30.4	0.10	81.4

biofuel selectivity and reactant conversion were obtained at a reaction temperature of 400 °C. Thus, the activity test studies were carried out at 400 °C under atmospheric pressure. The activity test of all catalysts was investigated for a 180 min. The model bio-oil was prepared constantly by mixing its subcomponents as HPO, formic acid, and furfural. The synthetic bio-oil reactant mixture composition is HPO/formic acid/furfural: 2:4:3 by mass ratio. In our previous study, a non-catalytic thermal cracking process, defined as a blank bed, was also performed. Thermal treatment was applied to the bio-oil components, and low oligomerization, hydrogenation, and aromatization were observed [13]. In catalytic applications, fuel phase selectivity can be improved, and bio-oil deoxygenation performance can be increased. The conversion values of the catalysts are presented in Table 5, with overall conversion values ranging from 46.1 to 83.8%.

The influence of calcination temperature on catalytic activity was also examined for the $LaFeO_3$ catalyst using ethanol as a co-reactant. Increasing the calcination temperature from 700 to 800 °C improved the crystallinity of $LaFeO_3$ (crystal size: 44.5 → 67.6 nm), which reduced lattice microstrain and resulted in higher catalytic activity and overall conversion from 69.4 to 83.4%. An increase in overall conversion promoted the formation of the targeted oil-phase products, leading to an increase in yield from 56.1 to 67.0%. $LaFeO_3$ exhibited superior upgrading performance, mainly due to its orthorhombic perovskite lattice structure and its mild surface acidity, which facilitate the activation and conversion of oxygenated

Table 5 Conversion values of reactants over bio-oil upgrading catalysts ($P = 1$ atm; $T = 400$ °C; 0.5 g catalyst; total gas flow rate 90 mL/min; reaction time: 180 min)

Catalyst	Conversion, %					Yield, %
	Alcohol	Formic Acid	HPO	Furfural	Overall	
Blank bed*	40.0	46.0	52.0	45.0	45.0	35.5
$LaFeO_3$ (700 °C)	62.0	63.2	88.7	57.7	69.4	56.1
$LaFeO_3$ (800 °C)	77.1	82.9	93.1	80.4	83.4	67.0
$LaFeO_3$ (800 °C-MeOH)	50.5	72.9	78.5	50.6	55.9	38.2
$LaFeO_3$ (24 h)**	76.5	81.5	91.3	80.0	82.5	66.0
$La_{0.9}Ce_{0.1}FeO_3$	76.5	81.1	92.1	84.2	83.8	65.8
$La_{0.8}Ce_{0.2}FeO_3$	69.8	75.3	86.6	69.0	75.2	56.6
$LaFe_{0.9}Co_{0.1}O_3$	19.7	44.2	92.8	69.7	57.9	40.8
$LaFe_{0.9}Mo_{0.1}O_3$	43.1	28.7	72.4	44.9	51.8	38.6
$LaFe_{0.9}W_xP_yO_3$	60.8	20.7	44.9	56.8	51.8	43.3
$La_{0.9}Sr_{0.1}FeO_3$	46.6	43.3	81.2	49.8	58.2	45.3
$La_{0.1}Sr_{0.9}FeO_3$	45.6	65.9	90.8	65.1	66.5	51.7
$La_{0.8}Ce_{0.2}Fe_{0.8}Co_{0.2}O_3$	19.3	29.9	84.9	50.6	49.2	34.7
α-Fe_2O_3	53.4	70.9	76.1	35.4	56.9	40.7
La_2O_3	43.2	58.3	71.7	16.4	46.1	28.5
α-Fe_2O_3/La_2O_3	58.2	42.9	70.6	64.6	62.7	42.8

*The catalyst was excluded during the blank bed experiment [13]

**The data obtained during the last 3-h period of the 24-h long-term stability test are presented

bio-oil compounds. Orthorhombic $LaFeO_3$ consists of corner-sharing FeO_6 octahedra, forming characteristic Fe–O–Fe bridging bonds that govern the oxygen mobility, and catalytic redox behavior of the perovskite framework. The more ordered perovskite lattice at 800 °C enhanced redox capability and strengthened Fe–O–Fe bonds, facilitating C–O bond cleavage and contributing to high overall conversion and iso-paraffin selectivity. Moreover, iso-paraffin selectivity increased from 65.3 to 69.4% when the calcination temperature was raised from 700 to 800 °C.

Methanol and ethanol which is $(H/C)_{eff}$ value of 2 are commonly used as co-reactants with bio-oil in the literature (Eq. (1)) [1, 7]. Thus, bio-oil dilutes the reactant medium, and the H_2 released during the co-cracking saturates the olefin chains. The effect of co-reactant was investigated in the presence of $LaFeO_3$ catalyst in the alcohol-assisted bio-oil upgrading study. In the experiment with methanol, the catalyst was named $LaFeO_3$ (800 °C -MeOH). Other reaction studies were carried out in the presence of ethanol. When methanol was used as a co-reactant on $LaFeO_3$, the overall bio-oil conversion was limited to 55.9%. Regarding bio-oil upgrading performance, high deoxygenation and high conversion values were achieved in the ethanol-assisted bio-oil upgrading study. The performance of the bare $LaFeO_3$ catalyst was limited in the presence of methanol. Ethanol was determined as a suitable diluent to carry out the cracking reaction with bio-oil in the presence of $LaFeO_3$-based perovskite. In addition, it is known from the literature that aldehyde groups indicate low-conversion biofuel production [7]. In biofuel production with upgrading, aldehyde groups cause coke formation. Therefore, low aldehyde conversion indicates that high amounts of coke are formed on the catalyst surface [13]. Thus, alcohol-assisted cracking is employed to increase the H/C_{eff} value of the reactant mixture. Hydrocarbon product distributions in methanol use as a co-reactant were examined to evaluate the effect on iso-paraffin and olefin selectivity. Due to methanol showing 50.5% conversion, the percentage of oxygenated compounds in the fuel phase was high at 45.6% by vol. The selectivity for iso-paraffin and olefin in the presence of MeOH was 29.9% and 22.4%, respectively. Although methanol and ethanol exhibit identical H/C_{eff} values, their catalytic behavior under co-cracking conditions differs significantly. The high iso-paraffin selectivity in the use of ethanol was observed with $LaFeO_3$ catalyst. Ethanol contains a C–C bond that undergoes β-scission, forming highly reactive radicals (e.g., $CH_3^{\cdot}$, $C_2H_5^{\cdot}$) that accelerate hydrogen transfer and the cracking of oxygenated bio-oil components [72, 73]. Methanol, mainly forms stable methoxy species and follows dehydration or reforming pathways [74, 75] instead of promoting chain scission. Methanol lacks C–C bond–derived radicals, resulting in limited hydrogen transfer and weaker cracking activity. Ethanol also adsorbs more strongly to metal oxides and perovskites, producing reactive intermediates such as ethoxy, acetate, and formate. Additionally, ethanol readily dehydrates to ethylene, promoting carbocation mechanism during cracking, isomerization, and oligomerization–cracking cycles that enhance olefin and iso-paraffin formation. Thus, despite their equal H/C_{eff}, ethanol provides a far more favorable medium for catalytic upgrading. The distribution of gas-phase products released during the activity tests with the co-cracking reaction is given in Table 6. Regarding deoxygenation capacity, CO_x selectivity in the presence of methanol was 23.29%, while it reached 68.14% in the presence of ethanol

component. The gas-phase product distributions presented in Table 6 indicate that the perovskite catalysts exhibit high deoxygenation performance in the presence of ethanol (EtOH). The CO_x product distribution in the gas phase ranged between 71.1 and ~56.4% for ethanol-assisted upgrading on perovskite. The presence of CO and CO_2 in the gas phase, resulting from the deoxygenation process, confirms a reduction in the oxygen content of the bio-oil. The detailed gas-phase product distribution values are provided in the Supplementary Information (Table S1).

It is reported in the literature that biofuel production via zeolite-catalyzed cracking reactions typically produces three distinct phases: an aqueous phase, an oil phase, and a gas phase. The desired main phase for biofuel is called the fuel phase. The aqueous phase consists of unreacted reactants and water produced as a by-product, whereas the gas phase mainly includes C_1–C_4 hydrocarbon by-products. On the other hand, the product distribution obtained using mesoporous catalysts exhibits distinct behavior; only oil and gas phases are observed, and no visible separation of an aqueous phase occurs [11]. In particular, this oil phase collected during the reaction also contains unreacted reactants. The liquid-phase products obtained in this study did not exhibit any visible phase separation. As a result, the collected liquid product was named as oil phase. The distribution of oil-phase products of perovskite-based catalysts and commercial metal oxides is given in Table 7. Analysis of the oil-phase composition was performed using a flame ionization detector (FID) coupled with an HP-1 capillary column. Oil-phase product composition is classified as n-paraffin, iso-paraffin, olefin, naphtha, aromatics, and oxygenated compounds

Table 6 Product distribution values of bio-oil upgrading catalysts in the gas phase

Catalyst	Product distribution, mol%	
	Total CO_x	Total C_1–C_4
Blank bed*	0.0	100.0
$LaFeO_3$ (700 °C)	71.14	28.86
$LaFeO_3$ (800 °C)	68.14	31.86
$LaFeO_3$ (800 °C-MeOH)	23.29	76.71
$LaFeO_3$ (24 h)**	67.06	32.94
$La_{0.9}Ce_{0.1}FeO_3$	65.82	34.18
$La_{0.8}Ce_{0.2}FeO_3$	67.50	32.50
$LaFe_{0.9}Co_{0.1}O_3$	56.39	43.61
$LaFe_{0.9}Mo_{0.1}O_3$	62.71	37.29
$LaFe_{0.9}W_xP_yO_3$	65.26	34.74
$La_{0.9}Sr_{0.1}FeO_3$	70.02	29.98
$La_{0.1}Sr_{0.9}FeO_3$	63.36	36.64
$La_{0.8}Ce_{0.2}Fe_{0.8}Co_{0.2}O_3$	60.66	39.34
α-Fe_2O_3	52.31	47.69
La_2O_3	14.61	85.39
α-Fe_2O_3/La_2O_3	64.26	35.74

*The catalyst was excluded during the blank bed experiment [13]

**The data obtained during the last 3-h period of the 24-h long-term stability test are presented

in terms of hydrocarbons. The iso-paraffin group is a desired hydrocarbon group in conventional gasoline fuel because it increases the octane number. Although both aromatic hydrocarbons and olefins contribute to an increased octane number, aromatic compounds are known to promote the formation of irregular emissions such as xylene, toluene, benzene, formaldehyde, and acetaldehyde and trigger the carbon deposition within the engine. On the other hand, olefins increase the volatile nature of the fuel, which requires limiting their concentration in commercial gasoline formulations [76]. Liquid aliphatic and aromatic hydrocarbons with carbon atoms ranging from C_4 to C_{12} are the source of gasoline, a petroleum-derived product [77]. The physicochemical properties of gasoline are closely linked to its hydrocarbon composition [78]. Enhancing the relative proportion of aromatic and iso-paraffin compounds is a common way to improve the octane number of gasoline [79].

La_2O_3 and α-Fe_2O_3 metal oxides were used individually or by forming a metal oxide mixture, and their comparisons with $LaFeO_3$ were also performed. In the presence of La_2O_3 catalyst, 14.6% CO_x selectivity and 46.1% overall bio-oil conversion were observed via bio-oil upgrading. Although the selectivity of the C_4 group, which indicates cracking and oligomerization in the gas-phase content, is high, when the fuel phase is examined, the oxygenated compound content is high due to the conversion values. α-Fe_2O_3, La_2O_3, and mixed α-Fe_2O_3/La_2O_3 catalysts showed lower conversion values in reactant components compared to $LaFeO_3$ perovskite. In the use of α-Fe_2O_3/La_2O_3 mixed oxide catalyst, overall bio-oil conversion was determined

Table 7 Product distribution and selectivity values of bio-oil upgrading catalysts in the oil phase

Catalyst	Product distribution, vol%						Oil-phase selectivity, %
	n-Paraffins	Iso-paraffins	Olefins	Naphthas	Aromatics	Oxygenated components	
Blank bed*	4.08	13.22	28.3	5.5	8.9	40.0	78.8
$LaFeO_3$ (700 °C)	0.01	65.3	22.7	4.4	5.8	0.8	80.8
$LaFeO_3$ (800 °C)	2.0	69.4	17.2	2.6	8.2	0.6	80.3
$LaFeO_3$ (800 °C-MeOH)	0.6	29.9	22.4	0.0	1.6	45.5	68.3
$LaFeO_3$ (24 h)	2.3	68.9	17.9	2.4	7.9	0.62	80.0
$La_{0.9}Ce_{0.1}FeO_3$	1.4	63.6	23.0	2.6	8.4	1.0	78.5
$La_{0.8}Ce_{0.2}FeO_3$	2.0	60.6	22.9	6.4	6.9	1.2	75.2
$LaFe_{0.9}Co_{0.1}O_3$	4.8	7.8	28.8	3.4	6.2	49.0	70.4
$LaFe_{0.9}Mo_{0.1}O_3$	0.5	0.8	8.6	11.5	2.2	76.4	74.6
$LaFe_{0.9}W_xP_yO_3$	1.1	78.1	10.6	4.9	4.2	1.1	83.5
$La_{0.9}Sr_{0.1}FeO_3$	9.1	7.3	16.8	3.0	3.7	60.1	77.8
$La_{0.1}Sr_{0.9}FeO_3$	12.0	8.8	15.2	4.0	7.4	52.6	77.8
$La_{0.8}Ce_{0.2}Fe_{0.8}Co_{0.2}O_3$	1.4	2.4	11.7	6.3	3.2	75.0	70.6
α-Fe_2O_3	2.6	47.5	25.5	9.1	14.4	0.9	71.6
La_2O_3	1.4	18.6	22.6	0.1	1.6	55.7	61.8
α-Fe_2O_3/La_2O_3	1.73	8.6	47.5	6.3	0.5	35.4	68.3

*The catalyst was not used in the blank bed experiment [13]

**The data obtained during the last 3-h period of the 24-h long-term stability test are presented

as 62.7%, and iso-paraffin and olefin selectivity was determined as 8.6% and 47.5% by volume, respectively. Thus, olefin content dominated the fuel phase, and a high oxygenated compound (35.4%) was observed. Low conversion values were observed due to coke accumulation on the surface of α-Fe_2O_3/La_2O_3 catalyst. Coke limited the activity of the catalysts and led to the formation of undesirable by-products. α-Fe_2O_3/La_2O_3 showed high activity in breaking C–C bonds, and coke blocked the pores of the catalyst. In particular, bare $LaFeO_3$ exhibited high coke resistance and high cracking performance compared to the α-Fe_2O_3/La_2O_3 mixed oxide catalyst.

When the oil-phase selectivities in Table 7 are examined, perovskite oxides generally exhibited high oil selectivity (between 68.3 and 83.5%). Sr, Mo, and Co doping in the perovskite structure caused high oxygen content in the fuel phase due to decreased reactant conversion values. In addition, the high values observed in the collected oil-phase selectivities are due to the presence of unconverted reactants since no phase separation is observed between the aqueous and oil phases. In the metal-doped $LaFeO_3$ catalysts, where the olefin hydrocarbon group content is higher in the oil-phase product distribution, the selectivity of saturated hydrocarbons (alkanes) in the gas-phase product distribution is also high. In this case, it can be said that the oligomerization reaction occurs with high performance, and therefore, the olefin selectivity is high in the oil phase. In the literature, Fe-based catalysts are used as selective catalysts for iso-paraffin production in the Fischer–Tropsch synthesis reaction [80, 81]. It was observed that there was a product distribution between iso-paraffin, olefin, naphtha, and aromatics in the presence of α-Fe_2O_3 catalyst. $LaFeO_3$ perovskite-based catalyst with orthorhombic crystal lattice structure exhibited high cracking, deoxygenation, bio-oil selectivity, and iso-paraffin selectivity compared to metal oxide catalyst. The usability of the $LaFeO_3$ catalyst was demonstrated in the bio-oil upgrading study carried out by the catalytic method. Various metal dopants were incorporated into the $LaFeO_3$ catalyst structure to investigate their influence on catalytic conversion and product selectivity. Ce incorporation stabilized the perovskite lattice and introduced oxygen vacancies, which accelerated the activation of C–O bonds in bio-oil molecules. Although the $La_{0.9}Ce_{0.1}FeO_3$ catalyst exhibits a lower surface area and smaller crystal size compared to bare $LaFeO_3$, it achieved the highest overall bio-oil conversion due to its enhanced oxygen mobility introduced by Ce doping. This improved lattice oxygen availability facilitated more efficient deoxygenation and cracking pathways. Moreover, its oil-phase selectivity (78.5%) was comparable to that of the undoped $LaFeO_3$ catalyst. However, as the Ce content ($x = 0.2$) increased, iso-paraffin selectivity in the oil phase decreased, while naphtha selectivity increased. This phenomenon was attributed to the formation of CeO_2 as a secondary phase within the catalyst structure. The increasing Ce ratio in the perovskite framework led to a higher concentration of the CeO_2 phase, which, in turn, enhanced naphtha selectivity. When the $La_{0.8}Ce_{0.2}FeO_3$ catalyst was used, naphtha selectivity reached 6.4%, while iso-paraffin selectivity was 60.7%. Isomerization and hydrogenation processes can further enhance iso-paraffin selectivity in the fuel phase. An increase in Ce loading resulted in reduced crystal size and pore diameter in the $La_{0.8}Ce_{0.2}FeO_3$ catalyst, which restricted the diffusion of bio-oil molecules and led to a decrease in overall conversion to 75.2%. At higher Ce contents, enhanced Ce^{4+}/Ce^{3+} redox

cycling and oxygen-vacancy sites facilitate controlled deoxygenation and hydrogen transfer reactions, stabilizing hydrocarbons in the naphtha range rather than promoting excessive cracking or aromatization. Additionally, the formation of a CeO_2 phase suppressed aromatic hydrocarbons while promoting naphtha-range products. Naphthene isomerization improves gasoline quality by increasing octane number and facilitating controlled aromatization pathways through enhanced hydrogen transfer reactions. Also, naphthene aromatization must be carefully controlled due to aromatic content limitations [82]. The highest iso-paraffin selectivity was obtained over the $LaFe_{0.9}W_xP_yO_3$ catalyst synthesized using TPA as the W precursor. Heteropoly acid incorporation was expected to introduce Brønsted acidity; however, after high-temperature calcination required for $LaFeO_3$ phase formation, partial decomposition of the Keggin structure likely occurred, leading to a reduction in the strong Brønsted acid sites. Simultaneously, W and P incorporation suppressed Lewis acid sites and cracking-active Fe–O–Fe linkages, thereby inhibiting deep cracking reactions. As a result, the overall conversion decreased due to limited cracking activity, while hydrogen transfer and saturation pathways were favored. This shift in reaction pathways promoted iso-paraffin formation, explaining the enhanced iso-paraffin selectivity despite the lower conversion observed for the TPA-doped catalyst. A literature survey has indicated that biofuel reaction catalysts have both Brønsted and Lewis acid sites for high catalytic performance [13, 30]. Doping the perovskite catalyst with Co, Mo, and Sr suppressed iso-paraffin content and shifted the product distribution toward other oxygenated compound groups. In Sr-doped $LaFeO_3$, partial substitution of La^{3+} by Sr^{2+} generates oxygen vacancies, which are intended to enhance the adsorption of oxygenated bio-oil species. This case significantly influences the adsorption kinetics of bio-oil molecules, particularly due to the weak acidic sites. Therefore, the cracking activity remains limited, resulting in the formation of an oxygen-rich fuel phase. In fact, in biofuel production via bio-oil upgrading, the reduction or removal of the high oxygen content is crucial for improving fuel quality. Since the conversion of ethanol used as a diluent for bio-oil decreases, the contribution of oxygenated compounds to the fuel phase appears to be high. The maximum oxygen content in the reformed gasoline is expected to be about 3.68% by weight [83]. Metal doping to the A and B sides suppressed the activity of $LaFeO_3$. Mo incorporation into the $LaFeO_3$ perovskite structure was intended to enhance redox behavior and facilitate C–O bond activation of oxygenated bio-oil compounds. Owing to its multiple oxidation states, Mo promotes oxygen-transfer reactions and surface activation of oxygenated bio-oil compounds. However, in the absence of sufficiently strong acidic sites and effective hydrogen transfer functionality, Mo-modified catalysts are considered to mainly favor partial deoxygenation pathways rather than deep cracking or complete oxygen removal. As a result, fuel phases with relatively higher oxygen content were observed, highlighting the role of Mo as a redox-active but selectivity-limited promoter in bio-oil upgrading. Although Mo is a widely used metal in the hydrodeoxygenation (HDO) reaction for bio-oil upgrading [84], it caused low paraffin selectivity and high oxygen compound formation in the co-cracking study. It has also been observed in the literature that the $CoAl_2O_4$ alloy formed in the catalyst structure improved activity and increased iso-paraffin selectivity. Co-containing alumina catalysts

improved the fuel properties and suppressed coke accumulation [13]. In Co-doped catalysts, the overall bio-oil conversion decreased, which can be attributed to insufficient deep cracking and limited C–O bond activation. The reduced performance of Co-doped catalysts is mainly associated with the absence of strong Brønsted acid sites and the limited strength of Lewis acidic centers. Thus, hydrogen-transfer-assisted secondary reactions are insufficient to further convert olefinic intermediates into saturated or aromatic hydrocarbons. Consequently, olefins accumulate in the product phase, while the overall conversion remains limited. Consequently, high oxygenated components content was observed in the fuel phase in Sr-, Co-, and Mo-doped $LaFeO_3$ catalysts. Unreacted ethanol and methanol can lead to high oxygen content in the fuel phase. In the cracking mechanisms of ketones, aldehydes, acids, and alcohols, it is generally accepted that oxygenated reactants initially undergo deoxygenation (through decarbonylation, decarboxylation, and dehydration) to form light olefins. These olefins can then undergo oligomerization to generate long hydrocarbon chains. Alkenes, in turn, may undergo hydrogenation or further aromatization to produce aromatic hydrocarbons [6]. The primary objectives in biofuel production from bio-oil are to enhance iso-paraffin selectivity in the oil phase, promote the formation of long-chain hydrocarbons, and effectively eliminate the oxygen content present in the bio-oil.

Moreover, based on the hydrocarbon distributions of the oil phase determined by detailed hydrocarbon analysis (DHA), the research octane number (RON) values were calculated using the DHA software in accordance with the ASTM D6729 standard approach. RON is a key indicator of fuel quality, reflecting the resistance of a fuel to engine knocking under spark-ignition conditions [85]. Therefore, the high RON value obtained in this study can be attributed to the favorable hydrocarbon distribution achieved over the $LaFeO_3$ catalyst, particularly the enhanced formation of iso-paraffins. RON is strongly influenced by the hydrocarbon composition of the fuel, with branched paraffins and aromatics generally exhibiting higher RON values than n-paraffins [86]. Oxygenated compounds, especially unconverted alcohol reactants that can overestimate RON values, were excluded from the RON evaluation. Based on the available data in this study, the theoretical RON value for the liquid phases obtained from the investigated catalysts was observed to be in the range of 72.4–94.8. The research octane number (RON) values of the oil-phase products with different catalysts are listed in Supplementary Information (Table S2). The oil phase produced over the $LaFeO_3$ (800 °C) catalyst in short-term activity showed a RON value of 94.8.

Additionally, 24-h stability assessment was conducted with the $LaFeO_3$ catalyst (calcined 800 °C), hereafter referred to as $LaFeO_3$ (24 h). Thus, the short-term and long-term performance of the $LaFeO_3$ catalyst was evaluated in this study. The stability of $LaFeO_3$ was evaluated through a long-term activity test conducted under continuous operation for 24 h at 400 °C and atmospheric pressure. Time-on-stream gas analyses were conducted every 30 min, and the obtained data were grouped into 3-h periods and reported as average values. Oil-phase analysis was performed by collecting samples over 3-h periods. The conversion, oil-phase selectivity, and the distributions of gas- and liquid-phase products obtained from the long-term experiment are presented in Fig. 11a–d. The long-term stability test revealed no catalyst

deactivation under the applied reaction conditions. Under identical reaction conditions, similar gas- and liquid-phase product distributions were observed in both short-term and long-term experiments. These results demonstrate that the $LaFeO_3$ catalyst exhibits high stability and strong resistance to coke formation. In addition, the catalyst continues to support biofuel production by preserving similar reaction pathways even after prolonged operation under reaction conditions. The oil-phase selectivity observed after the 24-h test indicates that the catalyst maintains its ability to direct the products toward the oil phase. Although minor variations in hydrocarbon distribution are observed, the overall distribution remains stable, with no significant changes among n-paraffins, i-paraffins, olefins, aromatics, or oxygenated compounds. During the final period of the 24-h test, iso-paraffin selectivity, oil-phase selectivity, and yield were determined as 68.9%, 80.0%, and 65.0%, respectively.

The experimental findings were assessed in the context of previously reported studies (Supplementary Information, Table S3). The reaction pressure was found to have a positive effect on improving bio-oil selectivity [1–3, 5, 6]. In addition, the use of ethanol as a co-reactant in bio-oil upgrading promoted the cracking pathways and suppressed coke formation on the catalyst surface. Moreover, mesoporous HZSM-5 and alumina-supported catalysts exhibited high catalytic activity in biofuel production. Different metals were incorporated into the structure of the silica microsphere catalysts (containing Ce, Mn) [44] and alumina-based catalysts (containing Co, W) [13] to improve coke resistance, cracking performance, i-paraffin selectivity, and surface acidity. However, as in the case of HZSM-5, excessively high

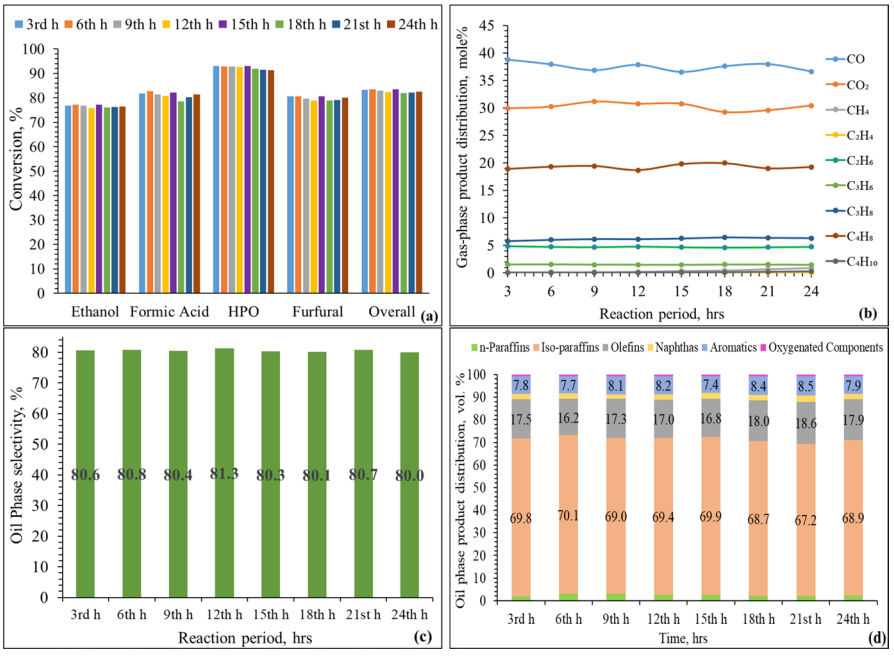

Fig. 11 Long-term stability performance of $LaFeO_3$: **a** conversion, **b** gas-phase product distribution **c** oil-phase selectivity, and **d** oil-phase product distribution

surface acidity may also induce coke formation, which in turn leads to a decline in catalytic performance [2, 11]. The cracking performance was strongly dependent on reaction pressure, temperature, and the compositional characteristics of the bio-oil feed. These parameters collectively governed the conversion, product selectivity, and the resulting product distribution.

Coke analysis of the spent catalysts

TG analysis determined the amount of coke deposited on the catalysts' surface. TGA was applied to spent catalysts in a dry air environment at temperatures ranging from 25 to 900 °C, with a heating rate of 10 °C/min. In TG analysis, the observed weight loss is attributed to the combustion of coke accumulated on the catalyst surface in the presence of oxygen in air. The TG analysis results of the spent catalysts, obtained after 3-h activity tests of the upgrading catalysts, are presented in Fig. 12a, b. In the TGA profiles, weight loss observed below 200 °C corresponds to the removal of physically adsorbed water and desorption of CO_2 from the catalyst surface. The weight loss of spent catalysts above 400 °C is due to the combustion of coke deposited on the catalyst surface. The weight loss of the spent catalysts above 400 °C is associated with the gasification of deposited coke through its oxidation to CO and CO_2. Previous studies indicate that amorphous carbon is oxidized below 500 °C, filamentous carbon between 500–650 °C, and graphitic carbon at temperatures above 750 °C [63]. Coke deposition on the catalyst surface occurs due to the Boudouard ($2CO \rightarrow C + CO_2$) and methane cracking ($CH_4 \rightarrow C + 2H_2$) reactions during biofuel production. These reactions lead to coke formation on the catalyst surface [13, 14]. The weak DTG responses below 500 °C in the perovskite catalysts signify the presence of amorphous carbon. When comparing the TGA results, the highest coke formation was observed in α-Fe_2O_3/La_2O_3 metal oxide catalyst (16.0 wt%). The α-Fe_2O_3/La_2O_3 catalyst prepared by a physical mixture exhibited high coke formation compared to perovskite-type $LaFeO_3$. Perovskite-based $LaFeO_3$ exhibited the highest catalytic activity regarding coke resistance and bio-oil cracking performance. In addition, the effect of the calcination temperature applied to the $LaFeO_3$ catalyst on activity was also investigated in this study. When the calcination temperature of bare $LaFeO_3$ increased from 700 to 800 °C, the coke formation in the spent catalyst structure was suppressed by decreasing from 0.45 to 0.24 wt%. The studies have resulted in obtaining biofuel with high bio-oil conversion, high selectivity, and minimized coke formation using the $LaFeO_3$ (800 °C) catalyst. However, the using of perovskite-based catalyst structure has significantly reduced the carbon content compared to metal oxide catalysts. The individual TGA/DTG profiles of the spent catalysts are provided in detail in the Supplementary Information (Fig. S1).

XRD analysis of spent catalysts was conducted to identify carbon deposits on catalyst surface, and the obtained XRD patterns are presented in Fig. 13a–c. In the XRD pattern of the spent catalysts, the weak peak at a 2Theta value of 26.6° was assigned to carbon (♠), indicating coke formation on the surface of the catalysts. In Fig. 13a, b, $LaFeO_3$-based perovskite catalysts have orthorhombic lattice structure in the patterns compatible with $LaFeO_3$ (●) (COD: 1526450). A characteristic peak of

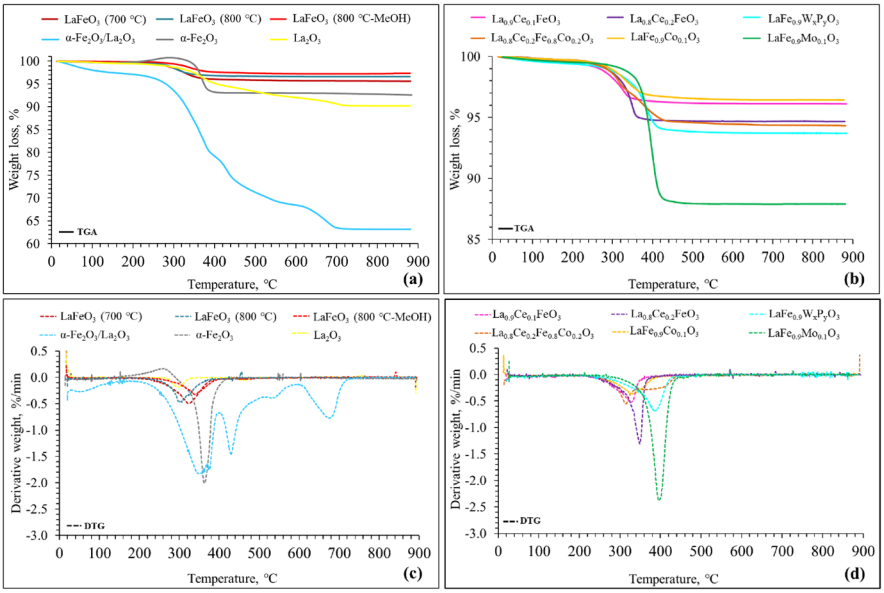

Fig. 12 **a**, **b** TG and **c**, **d** DTG profiles of the spent catalysts

cubic CeO_2 phase in $La_{0.8}Ce_{0.2}FeO_3$ catalyst (COD: 4343161 and JCPDS: 43-1002) was detected at 2Theta: 28.5°. The characteristic peaks in the XRD pattern of spent Fe_2O_3 catalyst in Fig. 13c correspond to the α-Fe_2O_3 (hematite, ▲) pattern (JCPDS No. 33–0664). The distinctive peaks associated with α-Fe_2O_3 appear at the following 2Theta ranges 35.7°, 37.4°, 43.4°, 53.9°, 57.4°, 62.9°, and 74.5° [87–89]. The XRD pattern depicted that the Fe_3O_4 (○) (JCPDS-82-1533) was additional peak as a secondary phase [90, 91]. During the analysis, the Fe_3O_4 phase (containing Fe^{2+}) present in the catalyst undergoes oxidation according to the oxidation reaction ($4Fe_3O_4 + O_2 \rightarrow 6\ Fe_2O_3$), which results in an increase in weight due to the incorporation of oxygen. Moreover, the Fe_2O_3 surface is known to adsorb active oxygen species in the temperature range of approximately 200–400 °C, which can further contribute to the observed weight gain [92]. $La(OH)_3$ (●) (COD: 4031381) phase and La_2O_3 metal oxide (■) (COD: 2002286) were observed in the XRD pattern of spent La_2O_3 metal oxide catalyst [69, 93]. The carbon peak related to coke formation was not observed in the α-Fe_2O_3 and α-Fe_2O_3/La_2O_3 XRD patterns. In the TGA results of the metal oxide catalysts, it was confirmed by Raman spectroscopy that the weight losses after 400 °C were due to coke.

Raman spectra of the metal oxide catalysts are given in Fig. 14. Characteristic peaks related to coke deposited were observed at 1378 cm^{-1} and 1594 cm^{-1}. The characteristic peak at about 1600 cm^{-1} indicates the G band, and the peak at 1387 cm^{-1} relates to the D band [94–96]. The deconvolution analysis of the D and G bands provides insight into the different types of carbon species present in the spent catalysts. Lorentzian functions were used to fit the peak profiles. Figure 14b–d illustrates the peak fitting results for the D and G bands. The Lorentzian curves obtained

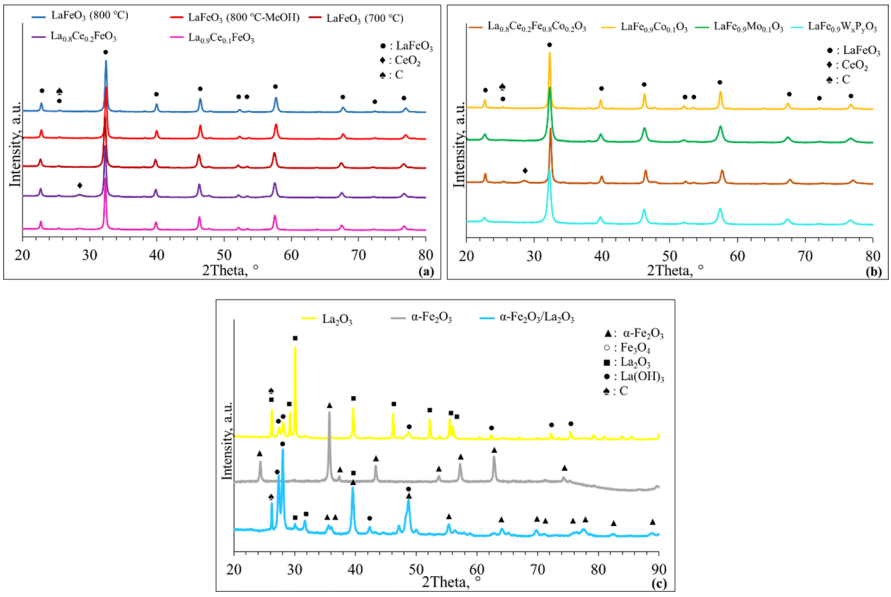

Fig. 13 The XRD pattern of **a**, **b** spent perovskite catalysts and **c** spent metal oxide catalysts

from the deconvolution are labeled as the D, D1, D2, D3, and G bands. The D band corresponds to defect-induced vibrational modes within the carbon network, arising from vacancies, heteroatom doping, or non-hexagonal ring structures, and is often associated with functional disturbances in the graphene layers. The D1-band is commonly attributed to a sp^2–sp^3 mixed carbon structure or an increased defect density, reflecting a higher degree of disorder. The D2-band observed at ~ 1518 cm^{-1} can be assigned to amorphous carbon, as this region typically corresponds to highly disordered or non-graphitic carbon species. The D3-band is similarly linked to disorder within the graphitic lattice and involves vibrations with E_2g_2 symmetry, indicating structural imperfections in graphitic domains. In contrast, the G band is the characteristic vibration of well-ordered sp^2-hybridized graphitic carbon. It arises from the in-plane stretching of C–C bonds in graphene layers (E_2g_2 symmetry) and serves as an indicator of graphitic ordering within the carbon lattice [97–101].

After a 24-h long-term stability test, characterization studies of the spent $LaFeO_3$ (24 h) catalyst were carried out (Figs. 15a–c and 16d). SEM analysis indicated that the surface morphology of the $LaFeO_3$ catalyst was preserved after the reaction (Fig. 15a). In the XRD pattern of the spent catalyst after the stability test, characteristic $LaFeO_3$ peaks (●) (COD: 1526450) indicating an orthorhombic lattice structure were observed. At the weak peak with a 2Theta value of 26.6°, the characteristic $LaFeO_3$ peak and carbon (♠) overlap (Fig. 15b). Therefore, Raman and TG/DTG analyses were also performed to determine coke formation on the catalyst surface. In the Raman spectrum of the $LaFeO_3$ catalyst used in the 24-h stability test, low-intensity D and G bands were observed at 1404 cm^{-1} and 1604 cm^{-1}, respectively (Fig. 15c). This indicates the presence of a limited amount of disordered and

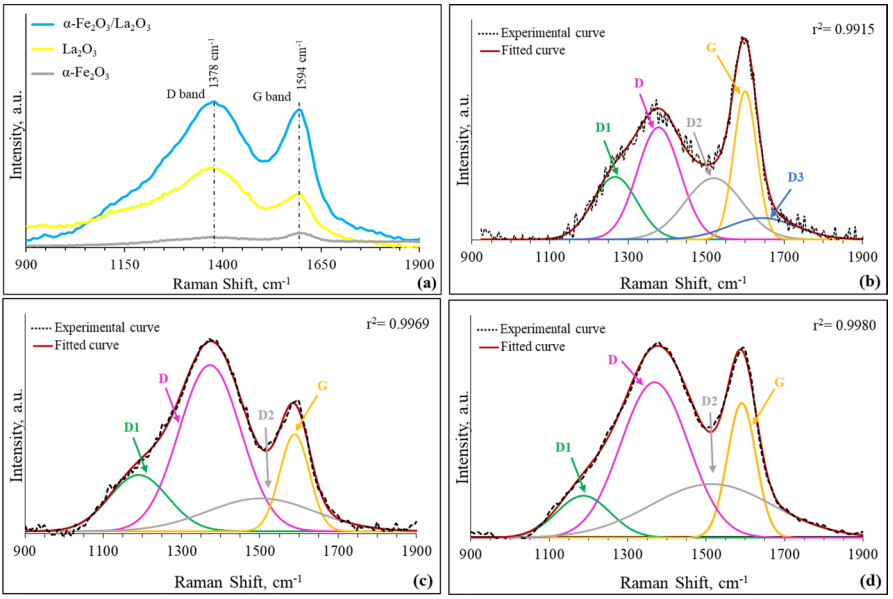

Fig. 14 **a** Raman spectrum of spent metal oxide catalysts, and deconvoluted Raman spectrum of **b** α-Fe_2O_3, **c** La_2O_3, **d** α-Fe_2O_3/La_2O_3 catalysts

graphitic carbon species. In contrast, the absence of detectable D and G bands in the Raman spectrum of the $LaFeO_3$ (3 h) catalyst (calcined at 800 °C) indicates that coke formation is highly suppressed under short-term reaction conditions (Fig. 15c). Consequently, the bulk perovskite structure of the spent $LaFeO_3$ catalyst was preserved after a long-term test.

To investigate the weight losses observed in the low-temperature region of the TGA profiles of spent perovskite catalysts, TG/DTG analyses were performed under different flow atmospheres (dry air and N_2) on spent $LaFeO_3$ (3 h) and $LaFeO_3$ (24 h) catalysts. In addition, the quartz chips (granular, 0.85–1.7 mm; Elemental Microanalysis) and quartz wool, which were placed in the reactor bed, were

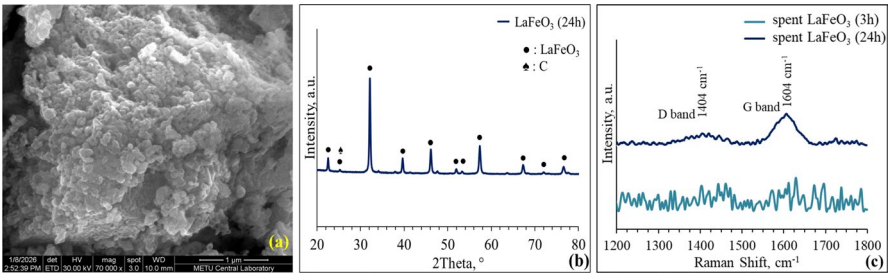

Fig. 15 **a** SEM images, **b** XRD pattern of the spent $LaFeO_3$ (24 h) catalyst, and **c** Raman spectra of the spent $LaFeO_3$ (24 h) and $LaFeO_3$ (3 h) catalysts

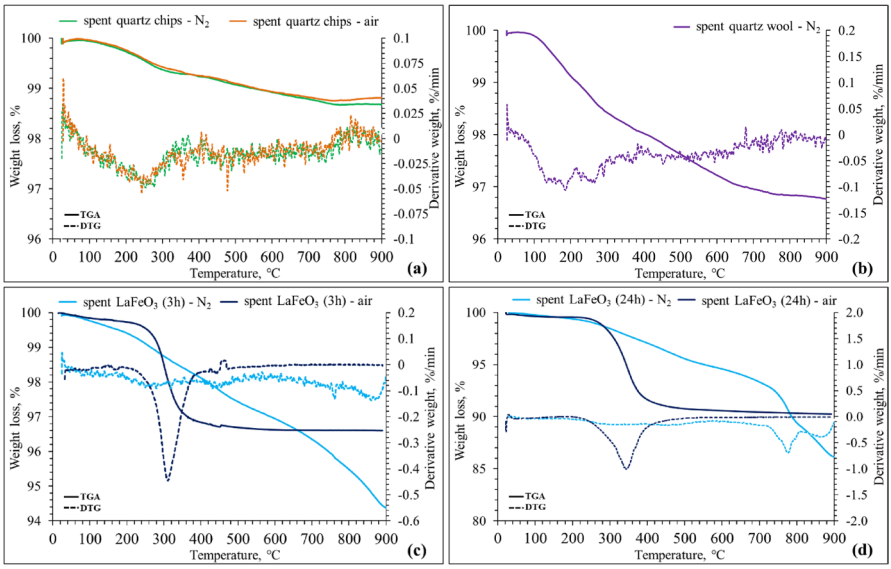

Fig. 16 TG-DTG profile of **a** spent quartz chips, **b** spent quartz wool, **c** spent $LaFeO_3$ (3 h) catalyst, and **d** spent $LaFeO_3$ (24 h) catalyst

exposed to the bio-oil upgrading reaction conditions and subsequently subjected to TG analysis under different flow atmospheres to verify the presence of coke on the catalyst structure (Fig. 16a, b). Based on examination of the TG profiles of spent quartz chips and spent quartz wool indicates that the observed weight losses arise primarily from bio-oil model residues in surface, strongly bound species, condensation products, partially polymerized bio-oil components, and oligomeric structures rather than coke combustion [102, 103]. Accordingly, these species were evaluated as surface residues rather than genuine coke deposits. In addition, the TG profiles obtained under an inert atmosphere are shifted to higher temperatures compared to those recorded under dry air conditions, while the corresponding DTG profiles exhibit broadening (Fig. 16a–d). Under an inert atmosphere, carbonaceous deposits do not combust; therefore, the observed weight losses are attributed to the desorption of adsorbed species or the thermal decomposition of soft carbonaceous residues rather than coke oxidation [104, 105]. In this study, weight losses observed above 400 °C in the TG profiles obtained under a dry air atmosphere were attributed to the formation of coke. Thus, a coke-related weight loss of approximately 1.39 wt% was observed for the spent $LaFeO_3$ (24 h) catalyst. Following the long-term stability test, the catalyst maintained stable performance with low coke deposition.

Conclusions

The upgrading of a model bio-oil mixture via co-cracking reaction was performed over $LaFeO_3$ perovskite-based and metal oxide catalysts. This study displays the synergistic effects of metal doping on $LaFeO_3$-based perovskite catalysts during ethanol-assisted bio-oil upgrading. The effects of using different co-reactants (MeOH and EtOH) and calcination temperatures on bio-oil upgrading performance of the $LaFeO_3$ catalyst were also investigated. Ethanol facilitated the cracking of oxygenated biofuel components and hydrogen transfer by producing highly reactive radicals. Moreover, ethanol was identified to be an effective co-reactant for bio-oil upgrading, contributing to enhanced iso-paraffin selectivity. The bare $LaFeO_3$ catalyst calcined at 800 °C demonstrated effective C–O bond cleavage during bio-oil upgrading, which was attributed to its strong Fe–O–Fe bridging bonds and well-ordered orthorhombic lattice structure. By increasing the calcination temperature from 700 to 800 °C, the overall conversion value increased from 69.4 to 83.4%. The perovskite-based $LaFeO_3$ catalyst showed superior resistance to coke formation compared to the α-Fe_2O_3/La_2O_3 catalyst prepared by physical mixing. Higher coke formation was detected in the α-Fe_2O_3/La_2O_3 catalyst (16.0 wt%) compared to the $LaFeO_3$ catalyst (0.24 wt%). The single-phase orthorhombic $LaFeO_3$ demonstrated high oil-phase selectivity, overall conversion and excellent deoxygenation performance. Thus, a high iso-paraffin selectivity of 69.4 vol% over $LaFeO_3$ was achieved. Metal doping into the $LaFeO_3$ lattice significantly altered the reaction pathways and fuel phase properties with the contribution of synergistic effects. The comparative evaluation of different metal dopants provides valuable insights into the adaptation of perovskite-based catalysts for selective bio-oil upgrading. The Ce doping in the $LaFeO_3$ structure has triggered olefin selectivity in the oil phase. When Co, Mo, Sr metals were doped into the perovskite structure, the iso-paraffin content was suppressed and replaced by oxygenated compound groups. Iso-paraffin selectivity improved with TPA doping as source of W, but the conversion values with coke formation (1.0 wt%) remained lower than pure $LaFeO_3$. The observed differences in catalytic performance are attributed to synergistic effects between the incorporated metals. In this study, the usability of the $LaFeO_3$ catalyst in a bio-oil upgrading study carried out by the catalytic method was demonstrated. Bare $LaFeO_3$ perovskite exhibited high cracking, deoxygenation, bio-oil selectivity, iso-paraffin selectivity, and low coke formation. Moreover**,** based on the 24-h long-term stability evaluation, the $LaFeO_3$ catalyst showed only minor carbon formation (1.39 wt%) and no signs of deactivation. The similarity in product distributions obtained from short-term and long-term tests indicates stable catalytic behavior under prolonged reaction conditions. The $LaFeO_3$ catalyst, characterized by its orthorhombic crystal lattice structure, demonstrated superior performance in terms of cracking efficiency, deoxygenation, bio-oil selectivity, and iso-paraffin selectivity when compared to conventional metal oxide catalysts. The potential applicability and efficiency of the $LaFeO_3$ catalyst were validated in bio-oil upgrading studies utilizing the catalytic co-cracking method. Consequently, the aim is to enhance C–O bond cleavage and iso-paraffin selectivity by introducing dopants that provide moderate acidity

without promoting excessive surface condensation or polymerization. The selective formation of iso-paraffins during bio-oil upgrading over perovskite-based catalysts can be effectively promoted through rational tuning of surface and structural properties. In particular, balancing the acid–base characteristics by controlling the strength and density of Lewis and Brønsted acid sites, together with suppressing excessive cracking activity, is essential to avoid deep fragmentation reactions. At the same time, appropriate metal doping that enhances hydrogen transfer, oxygen mobility, and redox functionality supports selective branching and hydrogenation pathways, thereby favoring iso-paraffin formation under moderate acidity conditions. We believe that proceeding while preserving the active sites of $LaFeO_3$ and without creating structural defects will be effective in terms of product selectivity and conversion.

Supplementary Information The online version contains supplementary material available at https://doi.org/10.1007/s11164-026-05936-x.

Acknowledgements This work was granted by the Scientific and Technological Research Council of Türkiye (TUBITAK)-ARDEB 1001 program (219Z232), TUBITAK BIDEB 2232 program (118C237), Gazi University Research Fund (FDK-2024-9608), Atılım University Research Fund (ATÜ-ADP-2021-03). Also, thanks to the TUBITAK-2211 PhD Scholarship Program and the TUBITAK-2250 Performance-Based Scholarships Program for PhD for their support. The authors thank the Central Laboratory of METU, KİTAM, AYBU and Atilim University Metal Forming Center of Excellence (MFCE) for the characterization results of the synthesized materials.

Author contributions Merve Celik Ozcan: Investigation, Validation, Methodology, Formal analysis, Visualization, Writing—original draft. Doruk Dogu: Investigation, Methodology, Supervision, Project administration, Writing—review & editing. Nuray Oktar: Investigation, Methodology, Supervision, Project administration, Writing—review & editing.

Funding Open access funding provided by the Scientific and Technological Research Council of Türkiye (TÜBİTAK).

Data availability No datasets were generated or analyzed during the current study.

Declarations

Conflict of interest The authors declare no competing interests.

Open Access This article is licensed under a Creative Commons Attribution 4.0 International License, which permits use, sharing, adaptation, distribution and reproduction in any medium or format, as long as you give appropriate credit to the original author(s) and the source, provide a link to the Creative Commons licence, and indicate if changes were made. The images or other third party material in this article are included in the article's Creative Commons licence, unless indicated otherwise in a credit line to the material. If material is not included in the article's Creative Commons licence and your intended use is not permitted by statutory regulation or exceeds the permitted use, you will need to obtain permission directly from the copyright holder. To view a copy of this licence, visit http://creativecommons.org/licenses/by/4.0/.

References

1. S. Wang, Q. Cai, X. Wang, Z. Guo, Z. Luo, Bio-gasoline production from co-cracking of hydroxypropanone and ethanol. Fuel Process. Technol. **111**, 86–93 (2013)
2. S. Wang, Y. Wang, Q. Cai, Z. Guo, Production of bio-gasoline by co-cracking of acetic acid in bio-oil and ethanol. Chin. J. Chem. Eng. **22**(1), 98–103 (2014)
3. S. Wang, Q. Cai, Z. Guo, Y. Wang, X. Wang, Renewable gasoline produced by co-cracking of methanol and ketones in bio-oil. Bioresour. **7**(4), 5019–5031 (2012)
4. S. Cheng, L. Wei, J. Julson, K. Muthukumarappan, P.R. Kharel, Upgrading pyrolysis bio-oil to biofuel over bifunctional Co-Zn/HZSM-5 catalyst in supercritical methanol. Energy Convers. Manag. **147**, 19–28 (2017)
5. S. Wang, J. Chen, Q. Cai, F. Zhang, Y. Wang, B. Ru, Q. Wang, The effect of mild hydrogenation on the catalytic cracking of bio-oil for aromatic hydrocarbon production. Int. J. Hydrogen Energy **41**(37), 16385–16393 (2016)
6. S. Wang, Q. Cai, J. Chen, L. Zhang, L. Zhu, Z. Luo, Co-cracking of bio-oil model compound mixtures and ethanol over different metal oxide-modified HZSM-5 catalysts. Fuel **160**, 534–543 (2015)
7. S. Wang, Q. Cai, X. Wang, L. Zhang, Y. Wang, Z. Luo, Biogasoline production from the co-cracking of the distilled fraction of bio-oil and ethanol. Energy Fuels **28**(1), 115–122 (2014)
8. P.S. Rezaei, H. Shafaghat, W.M.A.W. Daud, Production of green aromatics and olefins by catalytic cracking of oxygenate compounds derived from biomass pyrolysis: a review. Appl. Catal. A Gen **469**, 490–511 (2014)
9. Á. Ibarra, I. Hita, M.J. Azkoiti, J.M. Arandes, J. Bilbao, Catalytic cracking of raw bio-oil under FCC unit conditions over different zeolite-based catalysts. J. Ind. Eng. Chem. **78**, 372–382 (2019)
10. Q. Cai, J. Xu, S. Zhang, S. Wang, Aromatic hydrocarbon generation from a simulated bio-oil fraction by dual-stage hydrogenation-cracking: hydrogen supply and transfer behaviors. BioResources **12**(3), 5174–5195 (2017)
11. C. Guvenc, E. Alan, P. Degirmencioglu, M.C. Ozcan, B.P. Karaman, N. Oktar, Catalytic upgrading of bio-oil model mixtures in the presence of microporous HZSM-5 and γ-Al_2O_3-based Ni, Ta, and Zr catalysts. Fuel **350**, 128870 (2023)
12. S. Wang, Q. Cai, X. Wang, L. Zhang, Y. Wang, Z. Luo, Biogasoline production by co-cracking of model compound mixture of bio-oil and ethanol over HSZM-5. Chin. J. Catal. **35**(5), 709–722 (2014)
13. M.C. Ozcan, P. Degirmencioglu, E. Ekinci, B.P. Karaman, K. Murtezaoglu, N. Oktar, Effect of the amount and type of active metal and its impregnation sequence on bio-fuel production. Appl. Catal. A Gen. **683**, 119850 (2024)
14. B.P. Karaman, Nickel and cobalt incorporated mesoporous HZSM-5 catalysts for biofuel production from bio-oil model compounds. Res. Chem. Intermed. **50**(9), 4465–4483 (2024)
15. C. Liu, D. Chen, J. Ashok, P. Hongmanorom, W. Wang, T. Li, Z. Wang, S. Kawi, Chemical looping steam reforming of bio-oil for hydrogen-rich syngas production: effect of doping on LaNi0. 8Fe0. 2O3 perovskite. Int. J. Hydrogen Energy **45**(41), 21123–21137 (2020)
16. D. Gai, J. Shi, X. Cui, P. Zhao, W. Zuo, J. Zhang, G. Jia, Z. Huang, Catalytic performance and mechanism of A-site vacancy deficient perovskite catalyst over tar cracking during biomass pyrolysis. J. Clean. Prod. **405**, 136876 (2023)
17. S.N. Basahel, A.H. Medkhali, M. Mokhtar, K. Narasimharao, Noble metal (Pd, Pt and Rh) incorporated LaFeO3 perovskite oxides for catalytic oxidative cracking of n-propane. Catal. Today **397**, 81–93 (2022)
18. N. Hosseinpour, Y. Mortazavi, A.A. Khodadadi, Cumene cracking activity and enhanced regeneration of FCC catalysts comprising HY-zeolite and LaBO3 (B= Co, Mn, and Fe) perovskites. Appl. Catal. A Gen. **487**, 26–35 (2014)
19. M. de Santana Santos, R.C.R. Neto, F.B. Noronha, P. Bargiela, M.D.G.C. da Rocha, C. Resini, E. Carbó-Argibay, R. Fréty, S.T. Brandão, Perovskite as catalyst precursors in the partial oxidation of methane: the effect of cobalt, nickel and pretreatment. Catal. Today **299**, 229–241 (2018)
20. E.H. Yang, Y.S. Noh, G.H. Hong, D.J. Moon, Combined steam and CO_2 reforming of methane over La1-xSrxNiO3 perovskite oxides. Catal. Today **299**, 242–250 (2018)
21. S. Moogi, C.H. Ko, G.H. Rhee, B.H. Jeon, M.A. Khan, Y.K. Park, Influence of catalyst synthesis methods on anti-coking strength of perovskites derived catalysts in biogas dry reforming for syngas production. Chem. Eng. J. **437**, 135348 (2022)

22. P. Chen, J. Fang, Z. Zuo, C. Zhang, K. Wang, Z. Han, W. Tian, A review of perovskite catalysts for the simultaneous elimination of soot and NOx emissions from Diesel Engine. Sustainability **16**(23), 10793 (2024)
23. M. Theingi, K.T. Tun, N.N. Aung, Preparation, characterization, and optical property of $LaFeO_3$ nanoparticles via sol–gel combustion method. SciMedicine J. **1**, 151–157 (2019)
24. T. Liu, Y. Xu, Synthesis of nanocrystalline $LaFeO_3$ powders via glucose sol–gel route. Mater. Chem. Phys. **129**(3), 1047–1050 (2011)
25. U. Ozkan, S. Gunduz, D. J. Deka, Materials for ammonia synthesis. U.S. Patent No. 2020/0224323 (2020)
26. A. Løken, S. Ricote, S. Wachowski, Thermal and chemical expansion in proton ceramic electrolytes and compatible electrodes. Crystals **8**, 365 (2018)
27. Y. Zhang, B. Jiang, M. Yuan, P. Li, W. Li, X. Zheng, Formaldehyde-sensing properties of $LaFeO_3$ particles synthesized by citrate sol–gel method. J. Sol-Gel Sci. Technol. **79**, 167–175 (2016)
28. A.A. Ansari, N. Ahmad, M. Alam, S.F. Adil, M.E. Assal, A. Albadri, A.M. Al-Enizi, M. Khan, Optimization of redox and catalytic performance of $LaFeO_3$ perovskites: synthesis and physicochemical properties. J. Electron. Mater. **48**, 4351–4361 (2019)
29. P. Sangnikul, C. Phanpa, R. Xiao, H. Zhang, P. Reubroycharoen, P. Kuchonthara, T. Vitidsant, A. Pattiya, N. Hinchiranan, Role of copper-or cerium-promoters on NiMo/γ-Al2O3 catalysts in hydrodeoxygenation of guaiacol and bio-oil. Appl. Catal. A Gen. **574**, 151–160 (2019)
30. P.M. Mortensen, J.D. Grunwaldt, P.A. Jensen, K.G. Knudsen, A.D. Jensen, A review of catalytic upgrading of bio-oil to engine fuels. Appl. Catal. A Gen. **407**(1–2), 1–19 (2011)
31. R.G. Kukushkin, O.A. Bulavchenko, V.V. Kaichev, V.A. Yakovlev, Influence of Mo on catalytic activity of Ni-based catalysts in hydrodeoxygenation of esters. Appl. Catal. B Environ. **163**, 531–538 (2015)
32. F. Shi, J. Wang, H. Wang, C. Liu, Y. Lu, X. Lin, D. Hou, C. Wen, S. Yang, C. Luo, Z. Zheng, Y. Zheng, Increased high selectivity light aromatics and furans production by co-feeding methanol to catalytic pyrolysis of cellulose with Lanthanum-Cerium bimetallic modified MCM-41 catalysts. J. Energy Inst. **108**, 101206 (2023)
33. H. Arbag, S. Yasyerli, N. Yasyerli, G. Dogu, T. Dogu, Enhancement of catalytic performance of Ni based mesoporous alumina by Co incorporation in conversion of biogas to synthesis gas. Appl. Catal. B Environ. **198**, 254–265 (2016)
34. S. Cheng, L. Wei, J. Julson, M. Rabnawaz, Upgrading pyrolysis bio-oil through hydrodeoxygenation (HDO) using non-sulfided Fe-Co/SiO_2 catalyst. Energy Convers. Manag. **150**, 331–342 (2017)
35. D. Gai, X. Shi, J. Shi, X. Cui, P. Zhao, Synergistic effects of strontium modified $LaNi_{0.8}Fe_{0.2}O_3$ catalysts on coal and bamboo co-pyrolysis tar catalytic cracking. Biomass Bioenergy **202**, 108189 (2025)
36. Y. Jin, F. Hu, W. Wang, W. Wang, J. Chen, X. Nie, Y. Wen, P. Wang, X. Zhang, Further insights into catalytic pyrolysis of industrial lignin over lanthanum ferrite perovskite. Fuel **376**, 132728 (2024)
37. W.M. Chen, B.D. Xi, M.Y. Ye, M.X. Li, J.Q. Hou, Y.F. Wei, C.Z. Yu, F.H. Meng, X. Dai, Nickel doped enhanced $LaFeO_3$ catalytic cracking of tar for hydrogen production. J. Anal. Appl. Pyrolysis **183**, 106825 (2024)
38. N. H. Othman, N. Rahmat, N. H. Alias, F. Marpani, Composite perovskite-based material for chemical-looping steam methane reforming to hydrogen and syngas. Hybrid Perovskite Compos. Mater., pp. 315–333. (Woodhead Publishing, 2021)
39. D. Dogu, K.E. Meyer, A. Fuller, S. Gunduz, D.J. Deka, N. Kramer, A.C. Co, U.S. Ozkan, Effect of lanthanum and chlorine doping on strontium titanates for the electrocatalytically-assisted oxidative dehydrogenation of ethane. Appl. Catal. B Environ. **227**, 90–101 (2018)
40. D.J. Deka, J. Kim, S. Gunduz, D. Jain, Y. Shi, J.T. Miller, A.C. Co, U.S. Ozkan, Coke formation during high-temperature CO_2 electrolysis over $AFeO_3$ (A= La/Sr) cathode: effect of A-site metal segregation. Appl. Catal. B Environ. **283**, 119642 (2021)
41. S. Toygun, G. Könecoglu, Y. Kalpakli, General principles of sol-gel. J. Eng. Nat. Sci. Sigma **31**, 456–476 (2013)
42. S. Boumaza, L. Boudjellal, R. Brahimi, A. Belhadi, M. Trari, Synthesis by citrates sol-gel method and characterization of the perovskite $LaFeO_3$: application to oxygen photo-production. J. Sol-Gel Sci. Technol. **94**, 486–492 (2020)
43. F. Zhang, X. Zhang, G. Jiang, N. Li, Z. Hao, S. Qu, H2S selective catalytic oxidation over Ce substituted $La_{1-x}Ce_xFeO_3$ perovskite oxides catalyst. Chem. Eng. J. **348**, 831–839 (2018)

44. B.P. Karaman, N. Oktar, F. Gulec, Synergistic Mn–Ce modification of mesoporous silica microspheres for deoxygenation of bio-oil to biofuel. J. Energy Inst. **124**, 102399 (2025)
45. M. Ismael, M. Wark, Perovskite-type $LaFeO_3$: photoelectrochemical properties and photocatalytic degradation of organic pollutants under visible light irradiation. Catalysts **9**(4), 342 (2019)
46. J.C. Bear, P.D. McNaughter, P. Southern, P. O'Brien, C.W. Dunnill, Nickel-doped ceria nanoparticles: the effect of annealing on room temperature ferromagnetism. Crystals **5**(3), 312–326 (2015)
47. K.S. Ranjith, P. Saravanan, S.H. Chen, C.L. Dong, C.L. Chen, S.Y. Chen, R.T. Rajendra Kumar, Enhanced room-temperature ferromagnetism on Co-doped CeO_2 nanoparticles: mechanism and electronic and optical properties. J. Phys. Chem. C **118**(46), 27039–27047 (2014)
48. X.P. Xiang, L.H. Zhao, B.T. Teng, J.J. Lang, X. Hu, T. Li, Y.A. Fang, M.F. Luo, J.J. Lin, Catalytic combustion of methane on $La_{1-x}Ce_xFeO_3$ oxides. Appl. Surf. Sci. **276**, 328–332 (2013)
49. P. Shikha, T.S. Kang, B.S. Randhawa, Effect of different synthetic routes on the structural, morphological and magnetic properties of Ce doped $LaFeO_3$ nanoparticles. J. Alloys Compd. **625**, 336–345 (2015)
50. H. Ren, Z. Wang, X. Chen, Z. Jing, Z. Qu, L. Huang, Effective mineralization of p-nitrophenol by catalytic ozonation using Ce-substituted $La_{1-x}Ce_xFeO_3$ catalyst. Chemosphere **285**, 131473 (2021)
51. W. Sun, H. Wei, A.L. Yang, C. Jin, H. Wu, Z.A. Xiong, C. Sun, Oxygen vacancy mediated $La_{1-x}Ce_xFeO_{3-\delta}$ perovskite oxides as efficient catalysts for CWAO of acrylic acid by A-site Ce doping. Appl. Catal. B Environ. **245**, 20–28 (2019)
52. M. Ahangari, E. Mahmoodi, N. Delibaş, J. Mostafaei, E. Asghari, A. Niaei, Application of $SrFeO_3$ perovskite as electrode material for supercapacitor and investigation of Co-doping effect on the B-site. Turk. J. Chem. **46**(5), 1723–1732 (2022)
53. M. Kaewpanha, T. Suriwong, W. Wamae, P. Nunocha, Synthesis and Characterization of Sr-doped $LaFeO_3$ perovskite by sol-gel auto-combustion method. J. Phys. Conf. Ser. **1259**(1), 012017 (2019)
54. M. Ghaffari, T. Liu, H. Huang, O.K. Tan, M. Shannon, Investigation of local structure effect and X-ray absorption characteristics (EXAFS) of Fe(Ti) K-edge on photocatalyst properties of $SrTi_{(1-x)F}ex_{O(3-\delta)}$. Mater. Chem. Phys. **136**(2–3), 347–357 (2012)
55. N. Koonsaeng, T. Thaweechai, A. Wisitsoraat, W. Wattanathana, S. Wannapaiboon, S. Chotiwan, C. Veranitisagul, A. Laobuthee, Preparation of Sr-doped $LaFeO_3$ by thermal decomposition of metal organic complex and their gas-sensing properties. SOJ Mater. Sci. Eng. **6**(1), 1–9 (2018)
56. A. Desgagnés, O.A. Sahraei, M.C. Iliuta, Improvement strategies for Ni-based alcohol steam reforming catalysts. J. Energy Chem. **86**, 447–479 (2023)
57. U.V. Ancharova, S.V. Cherepanova, Nano-domain states of strontium ferrites $SrFe_{1-y}M_yO_{2.5+x}$ (M= V, Mo; $y \leq 0.1$; $x \leq 0.2$). J. Solid State Chem. **225**, 410–416 (2015)
58. K. Wang, H. Niu, J. Chen, J. Song, C. Mao, S. Zhang, C. Chen, Facile synthesis of CeO_2-$LaFeO_3$ perovskite composite and its application for 4-(Methylnitrosamino)-1-(3-Pyridyl)-1-butanone (NNK) degradation. Materials **9**(5), 326 (2016)
59. S. Thirumalairajan, K. Girija, V.R. Mastelaro, N. Ponpandian, Photocatalytic degradation of organic dyes under visible light irradiation by floral-like $LaFeO_3$ nanostructures comprised of nanosheet petals. New J. Chem. **38**(11), 5480–5490 (2014)
60. H.P. Lin, C.C. Chen, W.W. Lee, Y.Y. Lai, J.Y. Chen, Y.Q. Chen, J.Y. Fu, Synthesis of a $SrFeO_{3-x}$/gC_3N_4 heterojunction with improved visible-light photocatalytic activities in chloramphenicol and crystal violet degradation. RSC Adv. **6**(3), 2323–2336 (2016)
61. H. Arbag, Effect of impregnation sequence of Mg on performance of mesoporous alumina supported Ni catalyst in dry reforming of methane. Int. J. Hydrogen Energy **43**(13), 6561–6574 (2018)
62. T. Vijayaraghavan, R. Sivasubramanian, S. Hussain, A. Ashok, A facile synthesis of $LaFeO_3$-based perovskites and their application towards sensing of neurotransmitters. ChemistrySelect **2**(20), 5570–5577 (2017)
63. M.C. Ozcan, B.P. Karaman, N. Oktar, T. Dogu, Dimethyl ether from syngas and effect of CO_2 sorption on product distribution over a new bifunctional catalyst pair containing STA@SBA-15. Fuel **330**, 125607 (2022)
64. H.M. Tasdemir, The catalytic activity enhancement of commercial TiO_2 and Nb_2O_5 catalysts by iron for elemental sulfur production from H_2S. Catal. Lett. **149**, 473–485 (2018)
65. A. Bayat, T. Dogu, Optimization of CO_2/CO ratio and temperature for dimethyl ether synthesis from syngas over a new bifunctional catalyst pair containing heteropolyacid impregnated mesoporous alumina. Ind. Eng. Chem. Res. **55**(44), 11431–11439 (2016)
66. I.V. Kozhevnikov, Catalysis by heteropoly acids and multicomponent polyoxometalates in liquid-phase reactions. Chem. Rev. **98**(1), 171–198 (1998)

67. Y. Wang, J. Liu, W. Li, Synthesis of 2-butoxy ethanol with narrow-range distribution catalyzed by supported heteropolyacids. J. Mol. Catal. A Chem. **159**(1), 71–75 (2000)
68. B. Kalekar, N. Raje, A.V.R. Reddy, Solid state interaction studies on binary nitrate mixtures of uranyl nitrate hexahydrate and lanthanum nitrate hexahydrate at elevated temperatures. J. Nucl. Mater. **484**, 16–23 (2017)
69. A. Singh, V. Palakollu, A. Pandey, S. Kanvah, S. Sharma, Green synthesis of 1,4-benzodiazepines over La_2O_3 and $La(OH)_3$ catalysts: possibility of Langmuir–Hinshelwood adsorption. RSC Adv. **6**(105), 103455–103462 (2016)
70. J.G. Kang, Y.I. Kim, D.W. Cho, Y. Sohn, Synthesis and physicochemical properties of $La(OH)_3$ and La_2O_3 nanostructures. Mater. Sci. Semicond. Process. **40**, 737–743 (2015)
71. B.P. Gangwar, V. Palakollu, A. Singh, S. Kanvah, S. Sharma, Combustion synthesized La_2O_3 and $La(OH)_3$: recyclable catalytic activity towards Knoevenagel and Hantzsch reactions. RSC Adv. **4**(98), 55407–55416 (2014)
72. Z. Yu, S.S. Chuang, In situ IR study of adsorbed species and photogenerated electrons during photocatalytic oxidation of ethanol on TiO_2. J. Catal. **246**(1), 118–126 (2007)
73. N. Hansen, T.A. Cool, P.R. Westmoreland, K. Kohse-Höinghaus, Recent contributions of flame-sampling molecular-beam mass spectrometry to a fundamental understanding of combustion chemistry. Prog. Energy Combust. Sci. **35**(2), 168–191 (2009)
74. S.T. Yong, C.W. Ooi, S.P. Chai, X.S. Wu, Review of methanol reforming-Cu-based catalysts, surface reaction mechanisms, and reaction schemes. Int. J. Hydrogen Energy **38**(22), 9541–9552 (2013)
75. T. Omojola, A.J. Logsdail, A.C. Van Veen, S.A.F. Nastase, A quantitative multiscale perspective on primary olefin formation from methanol. Phys. Chem. Chem. Phys. **23**(38), 21437–21469 (2021)
76. S. Yitao, S. Shuai, W. Jianxin, X. Jianhua, Optimization of gasoline hydrocarbon compositions for reducing exhaust emissions. J. Environ. Sci. **21**(9), 1208–1213 (2009)
77. B.P. Vempatapu, P.K. Kanaujia, Monitoring petroleum fuel adulteration: a review of analytical methods. TrAC Trends Anal. Chem. **92**, 1–11 (2017)
78. C.R. Kaiser, J.L. Borges, A.R. dos Santos, D.A. Azevedo, A.D. Luiz, Quality control of gasoline by 1H NMR: aromatics, olefinics, paraffinics, and oxygenated and benzene contents. Fuel **89**(1), 99–104 (2010)
79. E. Stauffer, J. A. Dolan, R. Newman, Flammable and combustible liquids, in *Fire Debris Analysis*, pp. 199–233 (Elsevier, 2008)
80. J. Wei, R. Yao, Q. Ge, Z. Wen, X. Ji, C. Fang, J. Sun, Catalytic hydrogenation of CO_2 to isoparaffins over Fe-based multifunctional catalysts. ACS Catal. **8**(11), 9958–9967 (2018)
81. Y. Gao, L. Shao, S. Yang, J. Hu, S. Zhao, J. Dang, P. Yang, Recent advances in iron-based catalysts for Fischer–Tropsch to olefins reaction. Catal. Commun. (2023)
82. B. Makhlouf, Z. Abdelsadek, B. Hamada, P.J. Masset, Improvement of the octane number of petroleum naphtha using a molten salt based thermo-catalytic process. S. Afr. J. Chem. Eng. **52**, 170–182 (2025)
83. H. Chen, Lignocellulose biorefinery conversion engineering, in *Lignocellulose Biorefinery Engineering*, pp. 87–124 (Elsevier, 2015)
84. J.H. Lee, I.G. Lee, W. Jeon, J.H. Ha, K.Y. Lee, Catalytic upgrading of bio-tar over a MgNiMo/activated charcoal catalyst under supercritical ethanol conditions. Catal. Today **316**, 237–243 (2018)
85. Z. Wang, H. Liu, R.D. Reitz, Knocking combustion in spark-ignition engines. Prog. Energy Combust. Sci. **61**, 78–112 (2017)
86. H. Zhong, X. Song, S. He, X. Zhang, Q. Li, H. Xiao, X. Hu, Y. Wang, B. Chen, W. Li, Reaction behavior and kinetic model of hydroisomerization and hydroaromatization of fluid catalytic cracking gasoline. Molecules **30**(4), 783 (2025)
87. S. Liu, K. Yao, L.H. Fu, M.G. Ma, Selective synthesis of Fe_3O_4, γ-Fe_2O_3, and α-Fe_2O_3 using cellulose-based composites as precursors. RSC Adv. **6**(3), 2135–2140 (2016)
88. Y. Li, Z. Wang, R. Liu, Superparamagnetic α-Fe_2O_3/Fe_3O_4 heterogeneous nanoparticles with enhanced biocompatibility. Nanomaterials **11**(4), 834 (2021)
89. D. Aich, S. Saha, T. Kamilya, Synthesis and characterization of star shaped α-Fe_2O_3/Au nanocomposites. Mater. Today Proc. **43**, 1154–1159 (2021)
90. R. Das, C. Witanachchi, Z. Nemati, V. Kalappattil, I. Rodrigo, J.Á. García, E. Garaio, J. Alonso, L. Vu Dinh, L. Anh-Tuan, P. Manh-Huong, H. Srikanth, Magnetic vortex and hyperthermia suppression in multigrain iron oxide nanorings. Appl. Sci. **10**(3), 787 (2020)

91. T. Arun, K. Prabakaran, R. Udayabhaskar, R.V. Mangalaraja, A. Akbari-Fakhrabadi, Carbon decorated octahedral shaped Fe_3O_4 and α-Fe_2O_3 magnetic hybrid nanomaterials for next generation supercapacitor applications. Appl. Surf. Sci. **485**, 147–157 (2019)
92. G. Horvath, Z. Szalay, F. Simo, K. Salgo, F. Krcma, S. Matejova, Recycling of a wastewater to iron oxide micro structures. Environ. Res. Commun. **1**(8), 085001 (2019)
93. W.A. Adi, S. Wardiyati, S.H. Dewi, Nanoneedles of lanthanum oxide (La_2O_3): a novel functional material for microwave absorber material. IOP Conf. Ser. Mater. Sci. Eng. **202**(1), 012066 (2017)
94. L. Wang, Z. Li, C. Du, Y. Han, J. Yang, High-temperature graphitization of coke and lithium storage properties of coke-based graphite. Int. J. Coal Prep. Util. **44**(1), 19–36 (2024)
95. B.M. Vogelaar, A.D. van Langeveld, S. Eijsbouts, J.A. Moulijn, Analysis of coke deposition profiles in commercial spent hydroprocessing catalysts using Raman spectroscopy. Fuel **86**(7–8), 1122–1129 (2007)
96. S.M. Benoy, A. Hazarika, A. Rajbongshi, M. Bora, B.K. Saikia, Hierarchical porous carbon derived from petroleum coke via one-step chemical activation for the fabrication of a supercapacitor and real time clock application. RSC Adv. **14**(30), 21411–21424 (2024)
97. A. Ghosh, A.M. da Silva Santos, J.R. Cunha, A. Dasgupta, K. Fujisawa, O.P. Ferreira, A.O. Lobo, M. Terrones, H. Terrones, B.C. Viana, CO_2 sensing by in-situ Raman spectroscopy using activated carbon generated from mesocarp of babassu coconut. Vib. Spectrosc. **98**, 111–118 (2018)
98. D.G. Henry, I. Jarvis, G. Gillmore, M. Stephenson, Raman spectroscopy as a tool to determine the thermal maturity of organic matter: application to sedimentary, metamorphic and structural geology. Earth-Sci. Rev. **198**, 102936 (2019)
99. J.S. Lee, Y.K. Kim, J.Y. Hwang, H.I. Joh, C.R. Park, S. Lee, Carbon nanosheets by the graphenization of ungraphitizable isotropic pitch molecules. Carbon **121**, 479–489 (2017)
100. A.V. Ramya, A.N. Mohan, B. Manoj, Wrinkled graphene: synthesis and characterization of few layer graphene-like nanocarbons from kerosene. Mater. Sci.-Poland **34**(2), 330–336 (2016)
101. A.J. Cortés-López, E. Muñoz-Sandoval, F. López-Urías, Oxygenated surface of carbon nanotube sponges: electroactivity and magnetic studies. ACS Omega **4**(19), 18011–18022 (2019)
102. X. Guo, Y. Zheng, B. Zhang, J. Chen, Analysis of coke precursor on catalyst and study on regeneration of catalyst in upgrading of bio-oil. Biomass Bioenerg. **33**(10), 1469–1473 (2009)
103. A. Sanna, K. Ogbuneke, J.M. Andrésen, Bio-coke from upgrading of pyrolysis bio-oil for co-firing. Fuel **88**(12), 2340–2347 (2009)
104. Y. Elkasabi, A.A. Boateng, M.A. Jackson, Upgrading of bio-oil distillation bottoms into biorenewable calcined coke. Biomass Bioenerg. **81**, 415–423 (2015)
105. M.U. Garba, U. Musa, A.G. Olugbenga, Y.S. Mohammad, M. Yahaya, A.A. Ibrahim, Catalytic upgrading of bio-oil from bagasse: thermogravimetric analysis and fixed bed pyrolysis. Beni-Suef Univ. J. Basic Appl. Sci. **7**(4), 776–781 (2018)

Publisher's Note Springer Nature remains neutral with regard to jurisdictional claims in published maps and institutional affiliations.

Authors and Affiliations

Merve Celik Ozcan[1,2] · Doruk Dogu[3] · Nuray Oktar[1]

✉ Nuray Oktar
nurayoktar@gazi.edu.tr

Merve Celik Ozcan
celikmerve@gazi.edu.tr

Doruk Dogu
doruk.dogu@atilim.edu.tr

[1] Department of Chemical Engineering, Faculty of Engineering, Gazi University, Ankara, Turkey

[2] Department of Chemical Engineering, Graduate School of Natural and Applied Sciences, Gazi University, Ankara, Turkey

[3] Department of Metallurgical and Materials Engineering, Atılım University, Ankara, Turkey